CLIMATOLOGY

Denitrifying pathways dominate nitrous oxide emissions from managed grassland during drought and rewetting

E. Harris[1]*, E. Diaz-Pines[2], E. Stoll[1], M. Schloter[3,4], S. Schulz[3], C. Duffner[3,4], K. Li[5], K. L. Moore[5], J. Ingrisch[1], D. Reinthaler[1], S. Zechmeister-Boltenstern[2], S. Glatzel[6], N. Brüggemann[7], M. Bahn[1]

Nitrous oxide is a powerful greenhouse gas whose atmospheric growth rate has accelerated over the past decade. Most anthropogenic N_2O emissions result from soil N fertilization, which is converted to N_2O via oxic nitrification and anoxic denitrification pathways. Drought-affected soils are expected to be well oxygenated; however, using high-resolution isotopic measurements, we found that denitrifying pathways dominated N_2O emissions during a severe drought applied to managed grassland. This was due to a reversible, drought-induced enrichment in nitrogen-bearing organic matter on soil microaggregates and suggested a strong role for chemo- or codenitrification. Throughout rewetting, denitrification dominated emissions, despite high variability in fluxes. Total N_2O flux and denitrification contribution were significantly higher during rewetting than for control plots at the same soil moisture range. The observed feedbacks between precipitation changes induced by climate change and N_2O emission pathways are sufficient to account for the accelerating N_2O growth rate observed over the past decade.

INTRODUCTION

Nitrous oxide (N_2O) is a strong greenhouse gas and the most important stratospheric ozone-depleting substance emitted in the 21st century (*1*–*3*). The primary global source of N_2O is production during N cycling by microbiota in soils. Anthropogenic activities, in particular fertilizer use leading to an increase in reactive N (N_r) (*4*–*7*), have caused an increase in N_2O mole fraction from 260 to 270 nmol mol^{-1} in the preindustrial era to 331.7 nmol mol^{-1} today (*5*, *8*). Particularly concerning is the steep acceleration in growth rate from around 0.75 to above 1.0 nmol mol^{-1} a^{-1} over the past 10 years (*9*), which corresponds to an increase in emissions of 2 ± 0.4 Tg N_2O-N a^{-1} (section S1.1) (*8*, *10*). The causes of this acceleration, which is not explained by any steep rise in fertilizer use (*9*), are poorly known and could relate to the impact of climate change on emission processes. Climate change feedbacks could account for the recent increase in N_2O growth rate, as well as lead to further acceleration in the coming decades, affecting our ability to balance optimal fertilizer use for emission reductions and continuing food security (*7*, *11*, *12*).

N_2O is produced by soil microbes primarily during nitrification—an oxic process—and from denitrifying pathways, primarily under low oxygen conditions. Denitrifying pathways include heterotrophic denitrification (*13*), nitrifier denitrification (where ammonia oxidizer bacteria reduce nitrite) (*14*), and fungal denitrification, as well as minor pathways such as chemodenitrification (abiotic) and codenitrification (biotic), where an N atom from NO_2^- or NO combines with another N species—typically organic—to form N_2 or N_2O (*15*–*17*). These denitrifying pathways are hereafter referred to as "denitrification," with the specific subpathway given when relevant. In addition, heterotrophic denitrification can proceed to completion, consuming N_2O and reducing it to N_2 under low oxygen conditions (*18*, *19*). The balance between nitrification and denitrification in soils influences N_2O emission strength as well as affecting total reactive nitrogen loss, leaching, and fertilizer nitrogen (N) use efficiency, and thus controls environmental impacts of fertilizer N (*9*, *20*). Isotopic measurements may show an increase in the contribution of denitrification to global anthropogenic N_2O emissions over the past half-century with no well-identified cause (*21*). However, as the nitrification and denitrification pathways respond differently to environmental drivers, climate change impacts are challenging to predict, and models are currently unable to provide a robust assessment of emission feedbacks in the coming decades (*9*).

Climate change is expected to have strong impacts on precipitation regimes and thus causes major soil moisture anomalies—both positive and negative—in large areas of the globe (*22*–*24*). For grasslands in many regions, including the European Alps, a predicted increase in extreme summer droughts and an increased autumn-winter precipitation will represent a critical disturbance for ecosystem functioning and nutrient cycles (*25*–*28*). Soil moisture has consistently been shown to be one of the most important parameters affecting soil oxygenation and thus determining N_2O production rates from nitrification, denitrification, and other pathways (*13*, *29*–*31*). During drought, microbial activity and N_2O emissions are reduced (*32*–*35*). As soils are well oxygenated during drought, these low N_2O emissions are expected to result from nitrification, leading to nitrate accumulation; however, direct evidence for this assumption is missing. Rewetting after droughts usually causes large, fast pulses in N_2O fluxes (*27*, *34*, *36*)—"hot moments"—because of nitrogen

[1]Plant, Soil and Ecosystem Processes Research Group, Department of Ecology, University of Innsbruck, Sternwartestrasse 15, 6020 Innsbruck, Austria. [2]Institute of Soil Research, University of Natural Resources and Life Sciences, Vienna, Peter-Jordan-Straße 82, 1190 Vienna, Austria. [3]Research Unit Comparative Microbiome Analysis, Helmholtz Zentrum München, Ingolstädter Landstraße 1, 85764 Neuherberg, Germany. [4]Chair of Soil Science, Technical University of Munich, 85354 Freising, Germany. [5]Department of Materials, Photon Science Institute, The University of Manchester, Oxford Road, Manchester M13 9PL, UK. [6]Geoecology, Department of Geography and Regional Research, Faculty of Geosciences, Geography, and Astronomy, University of Vienna, Althanstraße 14, 1090 Vienna, Austria. [7]Forschungszentrum Jülich GmbH, Institute of Bio- and Geosciences, Agrosphere (IBG-3), Wilhelm-Johnen-Straße, 52425 Jülich, Germany.
*Corresponding author. Email: eliza.harris@uibk.ac.at

substrate buildup; however, the processes driving these emissions are extremely challenging to characterize because of their highly dynamic nature (*35*, *37*–*39*). These pulses are expected to result from denitrification due to increased soil moisture, thus leading to gaseous loss of reactive nitrogen. Similarly, high soil moisture during periods of increased rainfall is expected to increase denitrification and affect the balance between N_2O production and consumption; however, there are few direct observations of pathways under differing soil moisture regimes (*40*, *41*). Soil properties such as bulk density and microaggregate physicochemical attributes will modulate the strength of coupling between precipitation changes and soil moisture, which will furthermore be dependent on microbial community composition and activity.

A detailed understanding of the impacts of climate change on coupling between soil macro- and microscale properties, microbial communities, and N_2O emission pathways is critical to drive accurate biogeochemical models (*7*) and to identify likely trajectories of N_2O emission dynamics from ecosystems under global change. However, there is a lack of studies integrating these parameters across spatiotemporal scales while providing sufficient time resolution to capture dynamic responses of N_2O emission pathways to experimental perturbations. The isotopic composition of N_2O can be particularly useful to distinguish between formation and consumption pathways (see fig. S2 and the "Describing N_2O isotopic composition" section) and to provide an integrated picture of N cycling.

The linear N_2O molecule has two distinct positions for isotopic substitution that can be measured accurately following recent developments in laser isotope spectroscopy (*40*, *42*, *43*). The difference in isotopic composition of these two positions—the isotopic "site preference" (SP)—is independent of the substrate isotopic composition and depends only on the reaction(s) forming and destroying N_2O (fig. S2). SP and $\delta^{15}N$ are particularly useful to determine the partitioning between nitrification, denitrification, and N_2O consumption when considered in combination with other tools to obtain complementary insights into underlying processes. Investigations of microbial community structure and activity using molecular ecology techniques can confirm the identity of genes and/or microbes involved in N transformations, for example, by using quantitative polymerase chain reaction (qPCR) to measure the abundances of key functional genes in response to experimental treatments (*44*, *45*). Spatial analysis techniques like NanoSIMS (Nanoscale Secondary Ion Mass Spectrometry) and STXM-NEXAFS (Scanning Transmission X-ray Microscopy - Near Edge X-ray Absorption Fine Structrure) can be used to show the distribution, speciation, and incorporation of elements in the soil matrix and within soil microaggregates (*46*–*48*). Measurements of soil substrate $\delta^{15}N$ and monitoring of ancillary environmental and climate parameters also provide key data to understand drivers of observed isotopic changes and estimate isotopic mass balances. A combination of multiple techniques provides a more detailed and robust view of the N cycle and N_2O processes than would be possible with any single approach.

Here, we investigate N_2O emissions and isotopic composition from subalpine grassland monoliths subjected to an extreme drought and subsequent rewetting, in comparison to control and increased precipitation treatments throughout a growing season. In a climate manipulation experiment, N_2O isotopocules were measured online using automated chambers coupled to an N_2O isotopic spectrometer, giving a measurement frequency of <17 min for emitted ("source") $\delta^{15}N$ and SP. These results allowed an unprecedented level of detail for the analysis of variability in N_2O production and consumption pathways in response to environmental parameters. We aimed to quantify the net effect of drought and rewetting on emissions and pathways, which is currently unknown, as previous studies have not allowed for quantification of emission pathways with sufficient time resolution (*13*, *38*, *49*, *50*). We tested the hypothesis that drought enhances nitrification and rewetting favors denitrification as the major source of N_2O emissions. Furthermore, we hypothesized that N_2O emissions during rewetting periods would be large and highly variable because of rapid utilization of N substrate built up during drought, and we expected to see a consistent increase in denitrification contribution with increasing soil moisture over all treatments. We expected that the impacts of precipitation on N_2O emission pathways would be mediated by soil microscale properties—investigated using NanoSIMS—as soil properties dictate water drainage through drought and during rainfall, and thus the nature of anoxic and oxic microsites in the soil, while the chemical environment will influence the availability of different N species through drought and rewetting.

RESULTS AND DISCUSSION

N_2O emission pathways in the pre-drought period

Sixteen intact monoliths were extracted from a lightly managed subalpine grassland and established at the University of Innsbruck for 5 weeks before the beginning of the drought experiment, during which time water-filled pore space (WFPS) was stabilized to 30 to 40% (Fig. 1 and fig. S8). Seven of the monoliths were subject to an extreme drought (D) (see section S1.4.2 for details on definition and strength of the drought treatment), while four control (C) monoliths received the mean precipitation and four wet (W) monoliths received 25% more than the mean precipitation (see the "Study design" section). Throughout the experiment, W monoliths produced significantly more N_2O than C monoliths, with a greater proportion from denitrification (section S1.4.4).

All monoliths were fertilized with 200 kg-N ha^{-1} as NH_4NO_3 7 to 10 days before onset of the drought as described in the "Study design" section, which increased N_2O fluxes from 0.21 to 1.15 nmol m^{-2} s^{-1}. An analogous unfertilized control watering showed no significant change in fluxes in the same period (Fig. 1 and fig. S9). Considering 0 to 90 days after fertilization—the main growing season (July to October)—1% of fertilizer N was released as N_2O, in good agreement with the Intergovernmental Panel on Climate Change (IPCC) default value of 1% (*51*). Over the first 2 weeks after fertilization, N_2O production from nitrification and denitrification for non-drought plots was relatively equal; however, 15 to 30 days after fertilization, N_2O from nitrification returned to prefertilization levels. Over the 90-day main growing season, 68% of fertilizer-induced N_2O was produced via denitrification. Similarly, soil ammonium concentration decreased in the weeks after fertilization, while soil nitrate concentration increased, as nitrate was produced from ammonium by nitrification soon after fertilization (labeled as "pre-drought" versus "peak drought" in fig. S10). $\delta^{15}N$ of soil nitrate increased, reflecting production from isotopically heavier ammonium, as well as preferential consumption or leaching of isotopically light nitrate. Changes in $\delta^{15}N$ of ammonium appear to primarily reflect strong isotopic fractionation favoring leaching of heavy ammonium. Our study reveals that N_2O source dynamics following fertilizer application lead to a shift from nitrification-dominated

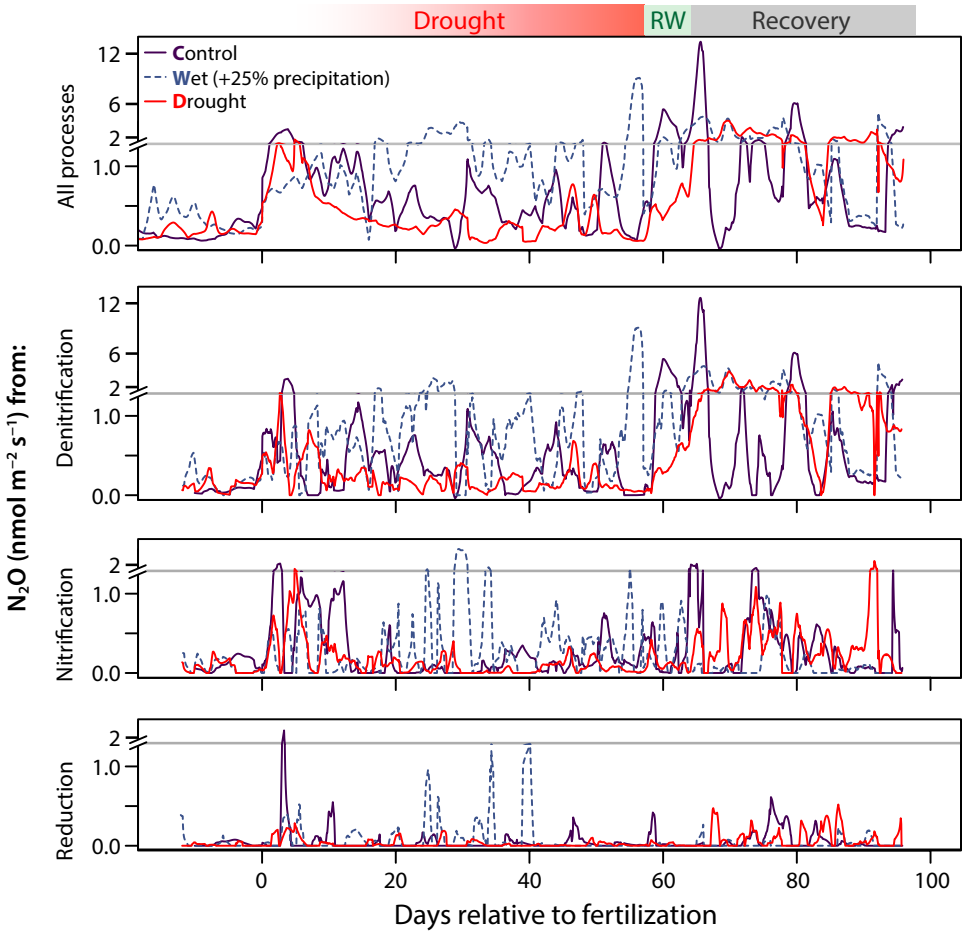

Fig. 1. Overview of N_2O fluxes from different pathways for control, wet (+25% precipitation), and drought treatments. The results are the 12-hour mean of all monoliths in a treatment group (n = 4,4, and 7, respectively). Fluxes were partitioned into pathways using "correlation partitioning model" (CPM; see the "Estimation of microbial N_2O production and consumption pathways: The CPM" section): "Denitrification" and "nitrification" refer to net N_2O production by the respective pathways, whereas "reduction" indicates N_2O consumption and production of N_2 during denitrification. The time axis is normalized to the date of fertilization, as this produces the largest single change in fluxes, and time periods for drought, rewetting (RW), and recovery are indicated at the top of the figure. The y-axis scale changes at 1.4 nmol m^{-2} s^{-1} as indicated to better capture the range of observed fluxes. The scales on all y axes are equal, but the maxima differ.

initially [as in (*52*); <10 days after fertilization] to denitrification-dominated when integrated over the entire growing season. These results complement the results of Castellano-Hinojosa *et al.* (*53*), who suggested that denitrification from deeper soil layers (15 to 20 cm) could dominate fertilizer-driven N_2O emissions after a year.

Impact of drought on N_2O emission pathways

Shortly after starting the drought treatment, N_2O fluxes dropped strongly, but then remained stable at 0.2 to 0.3 nmol m^{-2} s^{-1} below 30% WFPS (Figs. 1 and 2), with an average SP of <0‰ consistently measured for emissions below 30% WFPS. The lower source SP values measured for drought-stressed monoliths showed that the proportion of N_2O from denitrification increased under drought conditions. Denitrification produced 80 to 90% of N_2O between 20 and 30% WFPS, and around 70% of N_2O below 20% WFPS, despite little change in fluxes (Fig. 2). This pattern appeared stable across all monoliths, although isotope-based partitioning is relatively uncertain with low fluxes. N_2O reduction was not significantly affected by drought ($P > 0.05$). Although denitrification became somewhat more dominant during drought, drought did not induce a major shift in N_2O production pathways, in agreement with soil NO_3^-/NH_4^+ (fig. S10), which showed slower N turnover for drought monoliths (i.e., lower magnitude) but no difference in the direction of concentration or isotopic changes compared to controls. Similarly, drought had no consistent impact on absolute or relative abundances of functional genes involved in N_2O production (fig. S11), in agreement with the results of a recent meta-analysis (*35*). Thus, it appears that drought primarily affects N_2O by restricting the overall rate of N_2O production, most likely through reduced solute availability for all pathways (*54*).

Unexpectedly, very low WFPS did not reduce the proportion of N_2O from denitrification (low SP) pathways, although dry soils would be well oxygenated. This suggests that anoxic microsites remain present even in very dry soils, showing that reactive nitrogen loss to denitrification can continue throughout drought periods. NanoSIMS results at peak drought showed a strong enrichment of secondary ions indicative of nitrogen-bearing soil organic matter (N-SOM) (*47*, *48*) at the surface of drought treatment microaggregates (Fig. 3 and section S1.4.3), likely formed from nitrosation (addition of NO group) of SOM (*55*). Co-occurring buildup of sulfur and N-SOM

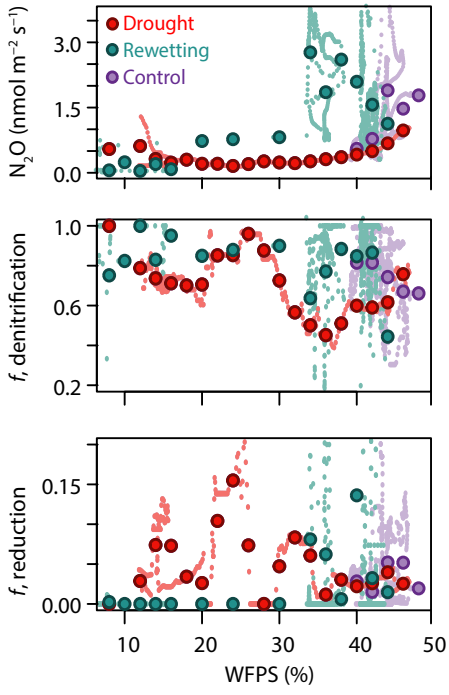

Fig. 2. Effect of reduced WFPS during the drought treatment ("drought," *n* = 7) and 0 to 15 days after the drought ("rewetting," *n* = 7) on N_2O fluxes and production pathways, compared to C/W monoliths ("control," *n* = 8). Large points show the mean value for all monoliths in each treatment for each 2% WFPS bin. Small paler points show individual 12-hour mean values.

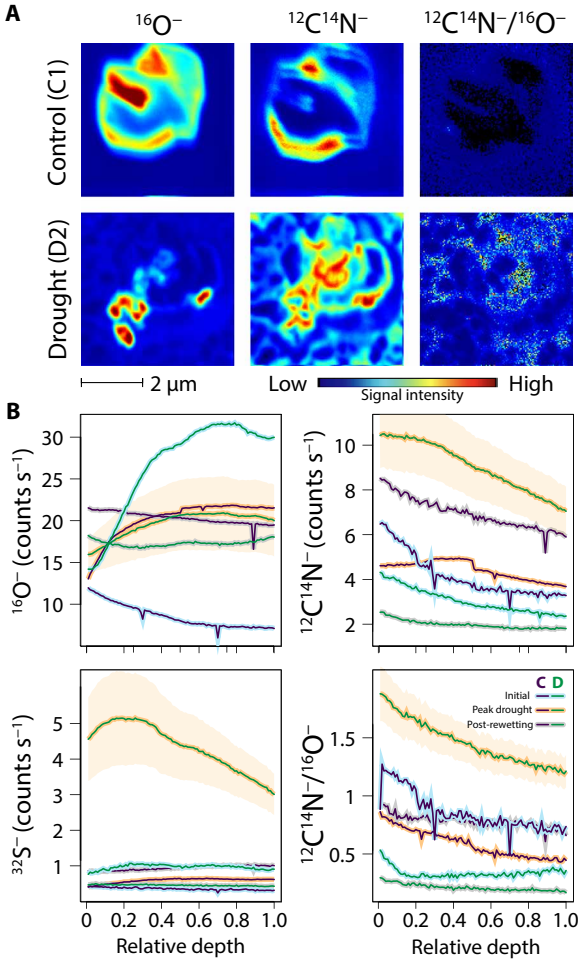

Fig. 3. NanoSIMS measurements comparing drought and control soil microaggregates, showing the enrichment in $^{12}C^{14}N^-$—indicative of organic N—relative to $^{16}O^-$ on drought soil grains. (**A**) Example NanoSIMS images of a typical control (monolith C1) and drought (D2) microaggregate soil grain showing $^{16}O^-$, $^{12}C^{14}N^-$, and ratio images. Signal intensity is shown on the color bar. (**B**) Average depth profiles for control and drought grains at initial, peak drought, and post-rewetting time periods (see section S1.4.3 for details and statistics). "Relative depth" on the *x* axis refers to layers sputtered away sequentially in NanoSIMS analysis normalized by dwell time as described in the "Estimation of microbial N_2O production and consumption pathways: The CPM" section. The standard error for the drought treatment at peak drought is shown as a shaded area; other error ranges are not included for clarity.

suggests that microbial cell death and subsequent release of organic components including S-containing amino acids could alternatively account for the changes in soil surface chemistry (*56*). Oxygen was not enhanced, thus suggesting that N-SOM was concentrated in an oxygen-deficient microenvironment under soil moisture deficit, providing a location for anoxic N_2O production to occur. During drought, soil microaggregates become increasingly hydrophobic (*57*, *58*); thus, microsites can retain water strongly and remain hypoxic, supporting anaerobic mechanisms.

The buildup of N-SOM leading to N_2O emissions during drought could be explained by the "codenitrification" or "chemodenitrification" pathways, whereby the N atom from NO_2^- or NO combines with an N atom from another species, particularly organic N, to form N_2O or N_2 by chemical or biotic N-nitrosation (*15*–*17*). This pathway is usually studied using isotopic labeling, as it results in "hybrid" N_2O, where labels show the incorporation of N from two different substrates (*59*). The SP of N_2O from chemo/codenitrification is not well constrained and depends on the substrates involved; previous results suggest that a pathway involving hyponitrous acid can produce N_2O with SP <0‰ (*60*), in line with the results of this study.

N_2O emission pathways following rewetting of soils

At the end of the drought treatment, the seven D monoliths were rewet in two groups 1 week apart (D1 and D2 treatments) to allow high time resolution for N_2O flux and isotope measurements. For comparison to the post-drought rewetting, a summary of N_2O flux effects from triweekly watering of the non-drought monoliths is given in section S1.4.4. The drought monoliths were rewet with varying amounts of rainwater (20 to 90 mm; see the "Study design" section) to achieve a rewetting gradient and assess potential nonlinearity in rewetting effects (*61*). However, each monolith took up water to increase WFPS by 25 to 30% to 31 ±4%, and the additional water leached out of the monoliths. Therefore, the rewetting gradient did not produce a gradient in soil moisture and thus did not cause variability in rewetting response.

Rewetting of the drought treatment monoliths significantly increased the N_2O flux as well as CH_4 uptake and CO_2 emissions, showing the expected pulse response often termed "Birch effect" (*62*, *63*) (fig. S12). N_2O emission peaks following rewetting were as high as 11.6 nmol m^{-2} s^{-1}, of which 92± 12% was due to denitrification, and they occurred 51 ± 12 hours after rewetting (Fig. 2 and fig. S12). Control monoliths were watered with 5.7 mm of rainwater

three times per week, including on the days when drought monoliths were rewet. On the first rewetting date, controls showed a strong watering response for both CO_2 and N_2O fluxes; however, this response was not seen for control monoliths on the second rewetting date (fig. S12). The rewetting peak was much larger than the average increase of 1.5 nmol m^{-2} s^{-1} seen following triweekly watering of control monoliths (fig. S7), and it also occurred much later (51 versus 12 hours), reflecting the significant stress of drought for the soil microbial ecosystem. Over the whole season, net emissions from control and drought plots were similar (0.124± 0.66 mmol m^{-2} for control and 0.121 ± 0.76 mmol m^{-2} for drought plots from mid-June to October); thus, reduced N_2O emissions during this extreme drought did not offset the effects of the rewetting peak.

N_2O emissions during rewetting were significantly higher for the same WFPS range than C or D emissions and highly nonlinear, illustrating hysteresis in the response of emissions to WFPS (Fig. 2). Hysteresis was also evident in the fraction of N_2O produced via denitrification, and the fraction of N_2O reduced: As WFPS increased during rewetting, more N_2O was emitted from denitrification than when WFPS decreased. Almost no N_2O reduction was evident in the correlation partitioning model (CPM) results during rewetting until WFPS was >30%, which suggests that initial rewetting emissions are from chemo- or codenitrification rather than from heterotrophic denitrification, as chemo- and codenitrification do not lead to N_2O reduction (*16*).

The drought-induced changes in soil microaggregate chemistry (Fig. 3) appear to be completely reversible, as no differences in elemental ratios were seen at the post-rewetting stage (table S3). Once water is available, N-SOM could be rapidly consumed via chemo- or codenitrification, thus accounting for some or all of the rewetting peak emissions and reversing the accumulation of N-SOM, after which heterotrophic or nitrifier denitrification once again dominates.

Abiotic versus biotic controls on N_2O emission pathways

WFPS was clearly the main driver of N_2O emissions throughout the drought-rewetting period (Fig. 2), displaying an exponential response of emissions to increasing WFPS despite minor changes in partitioning between production pathways. Triweekly watering of the control (C) and wet (W) monoliths provided further evidence of the nonlinear impact of WFPS on N_2O emissions (section S1.4.4). W monoliths (+25% precipitation; on average 3% higher WFPS) emitted 70% more N_2O from denitrification (1.2 versus 0.7 nmol m^{-2} s^{-1}) and 40% more from nitrification (0.31 versus 0.22 nmol m^{-2} s^{-1}), and thus a total average increase in N_2O fluxes of 55% for W compared to C monoliths (fig. S7).

Principal components analysis (PCA; Fig. 4) revealed additional controls on N_2O emissions. Before the drought, microbial functional gene abundances, bacterial biomass, and N_2O fluxes showed a strong positive relationship along PC1: Microbial functional gene abundances were clearly the main factor controlling N_2O emissions. Linear regressions confirmed that a strong relationship with N_2O fluxes was evident for *nirK* and *nirS* (nitrite reductase) abundances, which accounted for half of the variability in fluxes the week after fertilization (fig. S13). This supports the major contribution of denitrification evident from N_2O isotopocule measurements and CPM (see Fig. 1).

The PCA of factors controlling N_2O emissions through drought and rewetting showed clear differences to the initial period (Fig. 4). Microbial gene abundances were not a major factor controlling N_2O emissions during drought and rewetting, consistent with the results of (*49*). This was also evident in the pattern of microbial gene

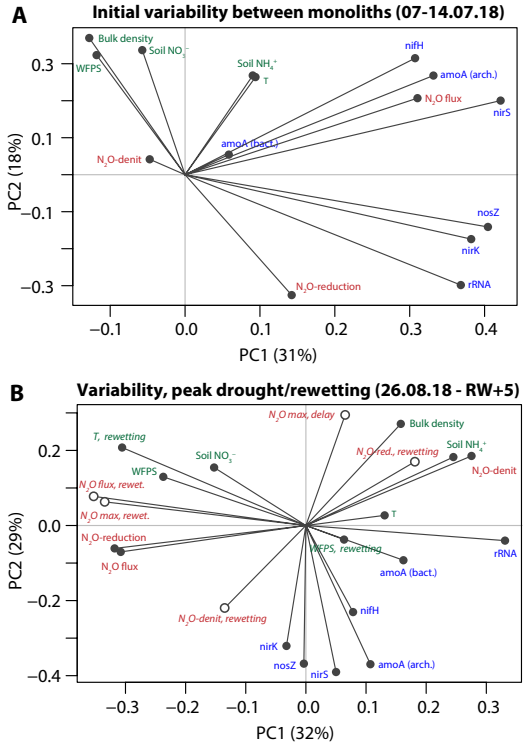

Fig. 4. PCA bi-plots describing the relationship between N^2O emission pathways and fluxes and explanatory variables. (**A**) before the drought experiment began, and (**B**) through peak drought (0 to 7 days before rewetting) and rewetting (0 to 7 days after rewetting). Soil parameters are shown in green, features of N_2O emissions are shown in red, and microbial functional gene abundances are shown in blue. In (B), parameters measured during the rewetting (from the rewetting to 7 days after) are highlighted with open circles and italic font to distinguish from parameters measured during the drought. "N_2O-denit" and "N_2O-reduction" refer to the proportion of N_2O produced/consumed by denitrification/reduction, respectively. "N_2O max, delay" refers to the time between rewetting and maximum N_2O flux.

abundance throughout the experiment, which showed no clear drought-induced decrease (fig. S11), despite much lower N_2O fluxes. Much weaker correlations between measured gene abundances and fluxes were observed in the drought and post-drought period (fig. S13), supporting the role of codenitrification, which is not represented in the measured genes, or chemodenitrification, which is not microbially mediated.

N_2O fluxes at peak drought and during rewetting, as well as the rewetting peak maximum, were strongly correlated with soil temperature at rewetting and WFPS before rewetting, as well as with soil bulk density and NO_3^- (PC1 in Fig. 4). PC2 revealed that a higher proportion of denitrification during rewetting was associated with higher fluxes, with a negative relationship to the delay between rewetting and peak fluxes. Overall, these results show that drought effects were more pronounced when bulk density was lower (*57*, *58*), which was expressed in lower N_2O flux and WFPS at the peak of the drought, and larger delay until peak N_2O occurred after rewetting. This controls the mean and maximum flux experienced after rewetting: Less severe drought effects led to a larger rewetting peak, with a larger denitrification contribution.

Our results showed an unexpected dominance of chemo- or codenitrification for N_2O emissions during drought in managed grassland soils, driven by the buildup of organic nitrogen. In contrast

to our initial hypothesis, drought did not promote nitrification: Although drought-affected soils are well oxygenated, substrate supply will limit N_2O production via the oxic nitrification pathway. As nitrite and N-SOM build up during drought, denitrifying pathways can continue, similar to previous observations in wetter soils (*64*, *65*). Although recent studies have highlighted the potential impact of alternative denitrification pathways (*15*–*17*), drivers and rates are poorly known, and thus, these pathways are not included in most models. A summary of driving factors found in this study is shown in Fig. 5. Constraining the contribution of these pathways to N_2O emissions and nitrogen loss in a changing climate will be a critical focus for future studies, particularly combining isotopic labeling and NanoSIMS approaches, to facilitate the addition of these relatively unknown pathways to biogeochemical models.

We found that drought and rewetting did not lead to an overall reduction in emissions across an entire season—for some drought monoliths, emissions were increased—despite strongly reduced fluxes in the drought period. This was due to hysteresis in the rewetting period causing emissions to overshoot the baseline WFPS-flux relationship (Figs. 2 and 5), in contrast to our initial hypothesis that emissions and pathways would exhibit a consistent response to WFPS. We observed that between monoliths in this experiment, increased drought severity reduced the size of the rewetting peak, contrary to expectations that continued fixation and nitrification during drought with reduced plant uptake would lead to an increased N_2O peak (*35*, *39*). This suggests the possibility for a "tipping point" for overall N_2O emissions in response to drought-rewetting cycles, whereby moderate droughts may increase total emissions, while severe droughts reduce emissions.

Recent results have shown a strong acceleration in N_2O growth rate in the past decade (*9*). In addition, tropospheric background isotopic measurements have shown a decrease in SP of the total anthropogenic source over the past half-century, from 18‰ [1940 to 2008 average; (*66*)] to 11‰ [2018; (*21*)], reflecting an increase in the contribution of denitrification to total anthropogenic emissions with no identified cause. Fertilizer use accounts for around half the increase in N_2O emissions since the preindustrial era (*7*), with a strong acceleration after 1950 and an ever increasing proportion of synthetic fertilizer (*67*). Our results show that synthetic NH_4NO_3 fertilizer can strongly promote denitrification over a growing season. If this result is representative of impacts in different soil types, the increasing use of synthetic fertilizers may explain the increased global contribution of denitrification to anthropogenic N_2O emissions over the past half-century—a trend that will likely continue. However, this cannot explain the acceleration in N_2O growth rate in the past decade (*9*), which is much faster than the global increase in fertilizer application over the same period.

The observed acceleration in N_2O growth rate requires a large increase in N_2O emission factors (*9*) that is likely to be driven by climate change impacts on N_2O pathways. Our results show that the relationship between N_2O and WFPS is exponential in these grassland soils (Figs. 2 and 5), thus suggesting that climate change–induced autumn-winter precipitation increases could strongly increase total N_2O emissions, and further contribute to large gaseous losses of reactive nitrogen. In this study, N_2O emissions were enhanced by 55% for +25% precipitation increase. We can gain a first estimate of potential global impact by considering the average flux density from croplands (0.24 ± 0.1 nmol m^{-2} s^{-1}) and from all ice-free land (0.04 ± 0.01 nmol m^{-2} s^{-1}) [annual averages, (*7*)], and assuming a similar

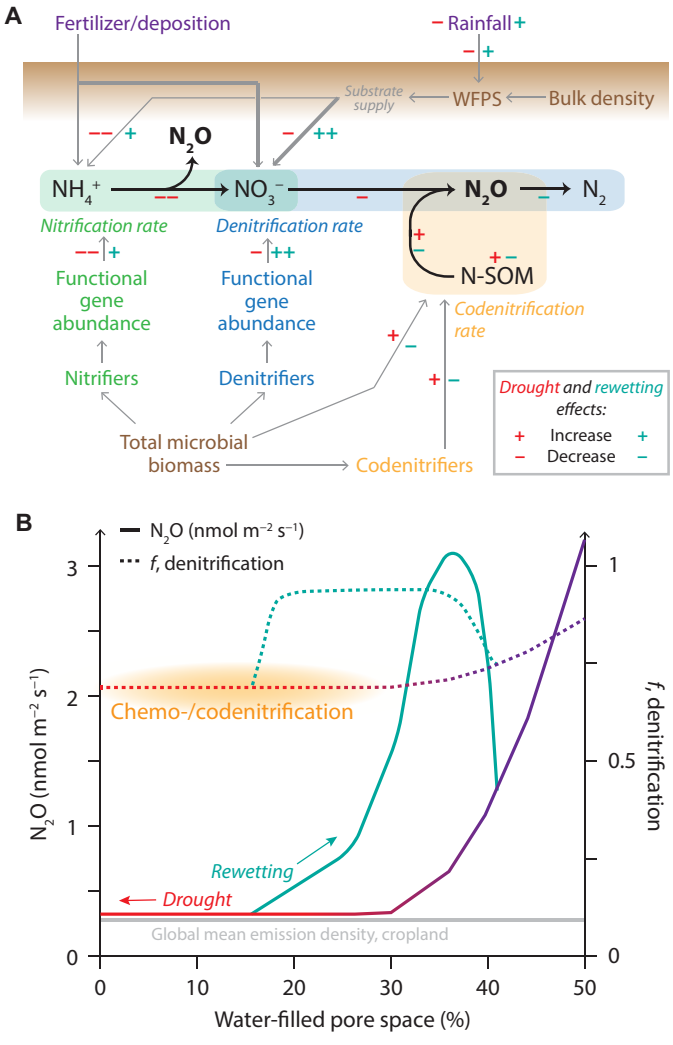

Fig. 5. Schematic view of the effect of soil moisture, drought, and rewetting on N_2O emissions and pathways, shown by this study for a drought experiment using managed subalpine grassland monoliths. (**A**) Linkages between key soil parameters regulating the emission of N_2O by different pathways are shown with gray arrows—thicker lines indicate a stronger relationship for some parameters. The impacts of drought are indicated in red and those of rewetting in green: + (++) signifies a (strong) increase, and – (– –) signifies a (strong) decrease. Inputs to the soil ecosystem are shown in purple and soil parameters in brown; microbial groups are shown with blue (nitrifiers), green (denitrifiers), and yellow (codenitrifiers). (**B**) Impact of WFPS on N_2O emission flux (solid lines) and the fraction of N_2O contributed by denitrification (dashed lines). The typical WFPS range is shown in purple, with the drought period highlighted in red and rewetting in green. The region where chemo-/codenitrification are important is highlighted in yellow. To illustrate the magnitude of the effects shown, the global mean emission density for croplands is shown in gray (*7*).

average sensitivity to increased precipitation across grasslands worldwide, which would need to be confirmed by further experimental studies of this type. In this case, just 2 months of +25% precipitation would increase N_2O emissions by 0.34 Tg N_2O-N a^{-1}, with equivalent losses of reactive nitrogen, which translates to an acceleration in growth rate of 0.04 nmol mol^{-1} a^{-1} (section S1.1). This shows the potential magnitude of climate feedback from a single mechanism [see also (*11*)]. Although numerous studies have shown the importance

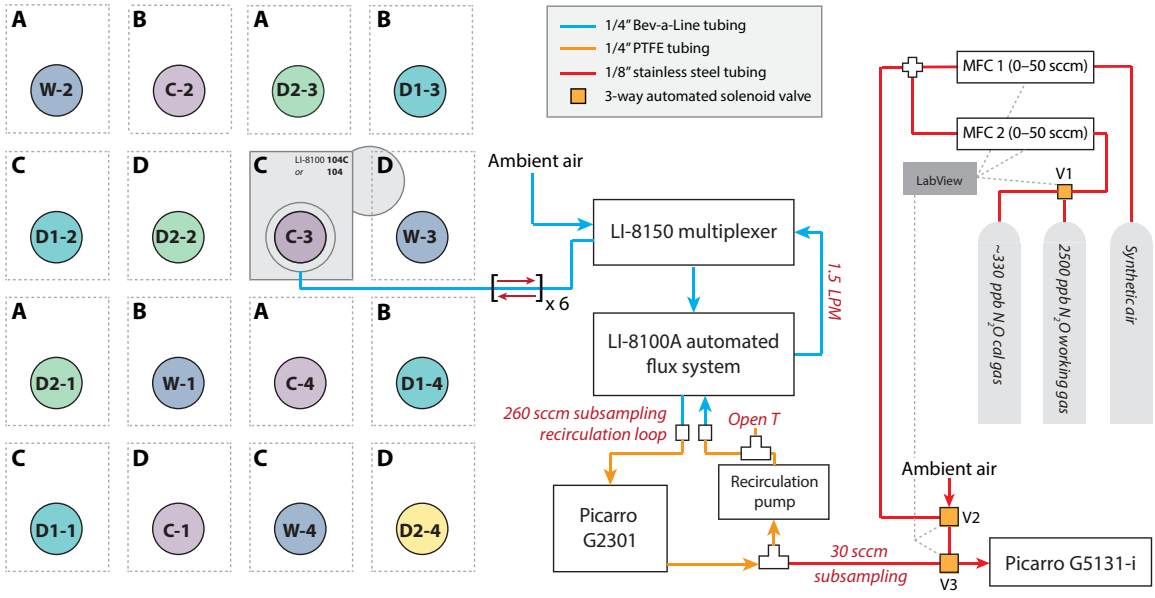

Fig. 6. A schematic view of the experimental setup showing the arrangement of the monoliths in the common garden, with the different treatment types indicated: C = Control (*n* = 4), W = Wet (*n* = 4), D1/D2 = Drought (*n* = 7). Monolith D2-4 received rain through the side of the tent and is therefore not included in subsequent analyses. An example footprint for an open chamber is shown for monolith C3, and measurement groups A to D are indicated for each monolith. On the right-hand side, the measurement setup including the calibration manifold is shown.

of soil moisture for N_2O emissions (*13*, *34*, *68*, *69*), few measurements have been made at low WFPS, and the nonlinear response of N_2O to WFPS has not been clearly evident in studies that consider smaller soil moisture ranges (*27*). Our results show that climate change, in particular precipitation changes, is the most likely cause of the recent acceleration in N_2O growth rate, illustrating the clear need for more mechanistic experimental studies of N_2O production pathways across ecosystems globally to improve model predictions of N_2O emissions in the future.

We show that denitrification via various mechanisms is responsible for most of the N_2O emissions from the managed grassland investigated in this study, and perturbations such as fertilization, drought, rewetting, or increased precipitation do not act to enhance the proportion of emissions from nitrification. The role of "minor" denitrification pathways such as chemo- and codenitrification is clearly critical and requires further investigation. Incorporation of these mechanistic results into biogeochemical models will improve the capability to understand and predict impacts of climate change feedbacks on N_2O emissions, thus facilitating sustainable policy development through targeted mitigation.

MATERIALS AND METHODS

Study design

Sixteen intact soil monoliths were collected from the Long-Term Ecosystem Research Carbon, Water and Nitrogen (LTER-CWN) subalpine meadow site Kaserstatt Alm in Stubaital, Austria (47°7′N, 11°18′E) located 1820 m above sea level (www.lter-austria.at/en/cwn-sites-stubai-valley/). The location has a mean inclination of 20°, mean annual temperature of 3°C, mean annual precipitation of 1097 mm, and dystric cambisol loam-textured soil. Further detailed information regarding vegetation and soil properties has been published previously (*70*–*73*). All major dates throughout the sampling and experimental period are summarized in table S1.

The 28-cm-deep monoliths were installed in 25-cm-diameter steel cylinders, with a rooting mat on a steel grate and 12-cm open space below each monolith for drainage and leachate collection. Monoliths were collected on 8 May 2018 and transported to Innsbruck on 14 May 2018. The steel cylinders containing the monoliths were placed in 30- to 35-cm-deep holes in the ground in a common garden adjacent to the measurement laboratory, as shown in Fig. 6. Transportation to Innsbruck involves a minor degree of warming compared to the Kaserstatt Alm site. However, in high alpine sites, actual canopy temperatures can be much higher than air temperatures because of high irradiance; thus, the temperature difference experienced by plants is far less than expected from air temperature differences (*74*). The observed effects of temperature on ecosystem functioning and microbial ecology for alpine grasslands are relatively minor (*74*–*76*); thus, the effects observed in this experiment are expected to be robust, and the logistical benefit of transporting to Innsbruck was essential to the experiment's success.

Soil water content (SWC) and temperature probes were installed in eight of the monoliths and programmed to measure every 15 min (HOBO Micro Station, Onset Computer Corporation, MA, USA). The probes were moved every 1 to 8 days throughout the experimental period so that data were regularly available for all 16 monoliths. In addition, relative humidity and air temperature were monitored at the surface and at 1.5 m above ground level, and photosynthetically active radiation was measured at 1.5 m (S-LIA-M003 and S-THB-M002, Onset Computer Corporation, MA, USA). Microclimate data were gap-filled for the times each monolith was not measured by interpolating the nearest measurements and overlaying the mean variability for the treatment group. Based on the measured SWC, monoliths were watered 150 to 300 ml up to three times a week to bring the SWC of each monolith to approximately 30% (gravimetric) before beginning of the experiment with fertilization in early July (see below).

The monoliths were assigned to treatment groups control (C), wet (W), and drought (D1/D2) at random, as well as into four measurement

groups designated A to D, where each had one monolith from each treatment. There were two drought treatment groups (D1 and D2) that were separately rewet so that emission dynamics following rewetting could be followed more closely (see the next section). For this study, drought is defined as a complete absence of precipitation, subsequently leading to stress and thus reduced biomass growth (*77*) discussed further in section S1.4.2. One monolith from treatment D2 (D2-4) was located at the edge of the rainout shelter and therefore received some rainfall during windy conditions—this monolith is not included in any subsequent analysis or discussion. On 2 July 2018, the eight monoliths in groups B and D were fertilized with 200 kg N ha^{-1} as NH_4NO_3 (BioXtra ≥99.5%, Sigma-Aldrich Inc., Germany) in 300 ml of water each; groups A and C monoliths were also watered 300 ml as a control comparison for fertilization. Fertilization was carried out for the eight monoliths in groups A and C on 5 July 2018 in the same manner. Fertilization was carried out in two blocks so that the N_2O dynamics following fertilization could be monitored with higher time resolution, as described in the next section.

On 11 July 2018, a rainout shelter was set up over all the monoliths using transmissive plastic greenhouse foil (Lumitec Clear AF, folitec Agrarfolienvertriebs GmbH, Germany) open at the bottom (approximately 0.5 m) to allow air circulation. Throughout the drought treatment, D1/D2 monoliths received no water, while C monoliths received the average rainfall for the region [884 mm; (*70*)] distributed evenly across 3 days per week: 5.7 mm/280 ml per watering. W monoliths received 25% more than the average precipitation: 7.1 mm/350 ml per watering. Both C and W monoliths are within the normal range of variability and are therefore used to provide a wide WFPS range as a baseline to consider drought impacts. On 3 September 2018, the drought was ended for "D1" drought monoliths (groups B/C) with 20 to 80 mm of collected rainwater added slowly over 45 min. On 11 September 2018, the drought was ended for "D2" drought monoliths (groups A/C) with 30 to 90 mm of collected rainwater. Following rewetting, D1/D2 monoliths were watered according to the control watering schedule until the rainout shelter was removed on 18 September 2018, after which all monoliths were exposed to natural precipitation.

Measurements of trace gas fluxes and N_2O isotopic composition

Describing N_2O isotopic composition

Isotopic composition is expressed as a "δ" value, which describes the deviation from an international standard

$$\delta^{15}N(‰) = \left(\frac{R_{sample}}{R_{standard}} - 1\right) \times 1000 \quad (1)$$

where $R = [^{15}N][^{14}N]$ and $R_{standard}$ is the isotopic ratio of atmospheric N_2 (AIR-N_2), or analogously for $\delta^{18}O$ (e.g., in NO_3^- or N_2O) using the O-isotope ratio of standard mean ocean water (V-SMOW). The linear N_2O molecule has two distinct positions for isotopic substitution—$^{14}N^{15}N^{16}O$ (α) and $^{15}N^{14}N^{16}O$ (β)—that can be measured accurately following recent developments in laser isotope spectroscopy (*40*, *42*, *43*). The bulk ^{15}N isotopic composition (hereafter $\delta^{15}N$) refers to the average $\delta^{15}N$ at both positions. The N_2O SP refers to the difference in ^{15}N isotopic composition between the central (α) position N and the terminal (β) position N (*78*)

$$SP = \delta^{15}N^{\alpha} - \delta^{15}N^{\beta} \quad (2)$$

Coupling of automated chambers and spectroscopic measurements

Measurements of CO_2, CH_4, and N_2O fluxes and isotopic composition were started on 15 June 2018 using the setup shown in Fig. 6. Six LI-COR chambers (8100-104 opaque long-term chambers and 8100-104C clear long-term chambers, LI-COR Inc., USA) were connected using 15-m tubing to the LI-COR LI-8150 Multiplexer followed by an LI-8100A automated flux system to monitor CO_2 using a flow rate of 1 liter min^{-1}. A subsample of 260 sccm (standard cubic centimeters per minute) from the outflow of LI-8100A was directed to a Picarro G2301 cavity ring-down spectrometer (CRDS; Picarro Inc., USA) system for the measurement of CO_2 and CH_4 in the chambers. Outflow from Picarro G2301 was split using a T-connection. Most of the air was returned to the chambers via a Vacuubrand A2000 Picarro recirculation pump—30 sccm was subsampled to a Picarro G5131*i* N_2O CRDS isotope analyzer and replaced with ambient air to avoid a pressure drop in the chamber system. As shown in Fig. 6, a combination of $^1/_4''$ Bev-A-Line tubing and $^1/_4''$ and $^1/_8''$ steel tubing connected with Swagelok fittings was used to interface the instrumentation. A chamber collar was installed on each of the 16 monoliths, and the chambers were moved between the monoliths every 1 to 5 days to obtain good data coverage on all monoliths.

For flux and isotope measurements, chambers were closed for 15 min, with 30-s flushing before and 45 s after each closure. In addition to chamber measurements, various calibration gases were measured:

1) AmbFS (ambient full system): Ambient air entering through LI-8150 and thus passing through the whole measurement system

2) AmbIso (ambient isotopic spectrometer): Ambient air entering directly into Picarro G5131*i*

3) MRDep (mixing ratio dependence): 2500 nmol mol^{-1} N_2O in synthetic air (Air Liquide Austria GmbH) diluted to approximately 300, 400, and 500 nmol mol^{-1} with synthetic air

4) Comp (compressed air): Medical compressed whole air (Air Liquide Austria GmbH)

The calibration setup used mass flow controllers (red-y SMART controller, GSC-A2SA-BB21, Vögtlin Instruments GmbH, Switzerland) and three-way solenoid valves (Burkert Austria GmbH) controlled with LabVIEW (National Instruments Inc., USA). A typical measurement sequence is shown in fig. S3. Including calibration as well as chamber and system flushing, every 6 hours and 40 min, all six chambers were measured four times, giving an average measurement frequency of 16.7 min.

Flux and isotope data processing and calibration

Measurement data were processed in blocks of 1 to 5 days, giving a balance between sufficient calibration points and required computing time. Data processing was carried out in R 3.5.1 (The R Foundation for Statistical Computing, 2018). Raw data from both Picarro instruments and a record of the calibration system (MFC flows, valve positions) from LabView were imported into R. CO_2 fluxes from LI-COR 8100A were first calculated from raw data using SoilFluxPro (LI-COR Inc., USA) using only the first 120 s of each chamber closure with a dead time of 20 s and imported into R to compare with data from the Picarro instrumentation.

The first step of data processing involved correction for MRDep of isotopic composition. The approximate time period corresponding to each (MRDep) measurement was found from the LabView record file. Within this time period, all MRDep data were first filtered to the target mixing ratio and then cut to include only the

flattest part of the "peak." These data were used to fit a linear model of N_2O mixing ratio versus $\delta^{15}N$ and SP and $\delta^{18}O$, which was calculated using the R function lm. If the correlation was significant ($P < 0.05$), the MRDep slope was used to correct all of the measurement data for the 1- to 5-day block including calibration gases and chamber measurements. Direct measurement of MRDep was only made after July 31 when the full calibration manifold was installed; before this date, the mean MRDep for August 1 to 15 was used to correct data. The mean mixing ratio and isotopic composition for the flat peak for each calibration measurement (AmbSys, AmbIso, MRDep, Comp) was calculated and used to produce a dataset as shown in fig. S3.

The fluxes of CO_2, CH_4, and N_2O for each chamber measurement were then found. First, the approximate time period was identified from the LI-COR data file and the LabView record file. Large changes in CO_2 mixing ratio at the start and end of each chamber measurement due to flushing were then used to identify the exact time when closed chamber air was present in Picarro G2301. An exponential model (*79*) was fit to the measurements and used to calculate the CO_2 flux using a dead time of 20 s and a maximum of 120 s of data

$$c_t - c_0 = \frac{Af}{V\lambda}(1 - e^{-\lambda t}) \quad (3)$$

where A is the chamber area, V is the system volume, t is the time, λ is a constant with units of time^{-1}, and c_0 and c_t are the CO_2 mixing ratios in the cell at initial time and at time t, respectively. When the exponential model failed to converge (<5% of measurements), a linear calculation was used. For both exponential and linear methods, fluxes were accepted at a confidence level of $P < 0.05$; measurements with no significant flux at $P < 0.05$ were designated as being below the detection limit. CH_4 and N_2O fluxes were calculated using the same method; however, all 15 min of chamber data was used. Convergence of the exponential model was worst for CH_4, because fluxes were lowest in magnitude relative to the CH_4 mixing ratio. The CO_2 fluxes from the Picarro G2301 data agreed very well with the fluxes from LI-COR 8100A calculated in SoilFluxPro, with R^2 of 0.75 to 0.95 and slopes of 0.8 to 1.1 for all data within each of the 1- to 5-day blocks. In all subsequent results and discussion, only CO_2 fluxes calculated from the Picarro G2301 data are shown.

The isotopic composition of source N_2O was calculated for each chamber closure using the Keeling plot method (*80*, *81*), which uses a plot of inverse chamber mixing ratio against measured isotopic composition to find the source isotopic composition as the intercept

$$\delta_{meas} = \frac{1}{m_{N_2O}} + \delta_{source} \quad (4)$$

where m is the mixing ratio and δ is the isotopic composition, e.g., $\delta^{15}N$. The 1-s raw isotopic data were very noisy; therefore, for the chamber closure, the data were first divided into six equal time blocks, and mean data were found for each block. The Keeling plot method was then applied to the six-block smoothed data to calculate the mean source isotopic composition. Error in the isotopic composition values (i.e., intercept) used the standard R algorithm for linear regression (lm). Isotopic composition values for the source were accepted if the Keeling plot regression was significant at $P < 0.05$ and the calculated error was less than 150‰. The constant 30-sccm dilution introduced into the system to balance the subsampling to Picarro G5131*i* (Fig. 6) was accounted for in flux and isotope data assuming that the added ambient air had the same mixing ratios and isotopic composition as measured ambient air; the total flow rate was 1 to 1.5 liters min^{-1}, so the effect of this correction was minor.

Following calculation of each 1- to 5-day block over the 5-month measurement period, all data were combined for postprocessing and calibration. Calibration to the international isotopic standard scale was accomplished by measuring two N_2O isotopic standards from Empa, Switzerland (Cal1 and Cal2; see table S2). These two standards were directly measured against the four calibration gas types in the "Measurements of trace gas fluxes and N_2O isotopic composition" section, as shown in table S2 (*82*). All chamber measurement data were corrected using a previously implemented approach described in detail in (*83*–*85*) and presented in brief here: AmbFS was first used as an anchor standard to correct drift in all measurement data by calculating deviations in AmbFS from its mean value and applying these to all data. Then, adjustment to the international standard scale was accomplished with a three-point calibration from AmbFS, Comp, and MRDep mean values over the entire measurement period. The final flux and isotope data were then filtered by removing outliers more than three SDs from the mean for each monolith. Of the total 9778 chamber measurements, 8202 (73%), 5341 (47%), and 4097 (37%) accepted values were obtained for N_2O flux and source $\delta^{15}N$ and SP, respectively. Details of the measurement precision and performance are given in section S1.4.1.

Estimation of microbial N_2O production and consumption pathways: The CPM

The microbial pathways contributing to N_2O production pathways can be estimated on the basis of measured fluxes and isotopic composition. Current literature estimates show some range in SP fractionation depending on experimental conditions, microbes studied, and other parameters such as pH, substrate, and substrate availability; thus, best estimates for the SP endmembers of denitrifying pathways (production) and nitrification were taken as $SP_D = -10‰$ and $SP_N = 30‰$, respectively (*86*). Fractionation factors of $\alpha_{SP} = -5.4‰$ and $\alpha_{15N-bulk} = -6.6‰$ were used for SP and $\delta^{15}N$ fractionation during N_2O reduction as the final step of heterotrophic denitrification (*18*, *86*). These isotopic fractionation factors will hereafter be referred to as "base values" to distinguish them from different isotopic values used in sensitivity studies discussed below.

As N_2O is reduced in the final step of denitrification, isotopically light N_2O and $N_2O - \beta$ are preferentially consumed; thus, the isotopic composition and SP of the remaining N_2O pool increase. It was therefore assumed that reduction activity would be evident as a negative correlation between SP and N_2O flux or a positive correlation between $\delta^{15}N$ and SP (*18*, *87*, *88*). To quantify contributions from each pathway to the final N_2O flux, the data were considered for each monolith separately in 12-hour blocks beginning every hour throughout the entire measurement period. If more than three simultaneous measurements of flux, $\delta^{15}N$, and SP were available within the 12-hour block, the correlations between $\delta^{15}N$ and SP, and flux and SP, were calculated using the R function lm. If either correlation was significant ($P < 0.05$) and positive/negative, respectively, it was taken as evidence for significant N_2O reduction. Several cases were considered:

1) If the mean SP within the block was lower than SP_D, denitrification was assumed to contribute 100% of N_2O with no N_2O reduction occurring.

2) If the mean SP within the block was between SP_D and SP_N but there was no evidence of reduction based on correlations between $\delta^{15}N$ and SP, and flux, the relative proportions of nitrification and denitrification were calculated using a mixing model with the two endmembers, where f_D is the fraction of N_2O contributed by denitrification, $f_N = 1 - f_D$, and SP_{mean} is the mean SP in the 24-hour window

$$f_D = \frac{SP_{mean} - SP_D}{SP_N - SP_D} \quad (5)$$

3) If the mean SP within the block was larger than SP_D and there was evidence for reduction, the measured slope between SP and $\delta^{15}N$ was compared to $\alpha_{SP}/\alpha_{15N-bulk}$ to determine the proportion of N_2O being reduced. For example, if a slope of 0.60 was measured for SP/$\delta^{15}N$, compared to $\alpha_{SP}/\alpha_{15N-bulk} = 0.82$, it was estimated that $\frac{(SP/\delta^{15}N)_{slope}}{\alpha_{SP}/\alpha_{15N-bulk}} = 0.60/0.82 = 73\%$ of the variability in isotopic composition was due to reduction ($f_{red} = 0.73$), with the remaining variability resulting from mixing between nitrification and denitrification. f_{red} was used to find SP_0 according to Rayleigh fractionation (*89*)

$$SP_0 = SP_{mean} - \alpha_{SP} \times \ln(1 - f_{red}) \quad (6)$$

where SP_0 is the SP of the directly emitted N_2O before any reduction took place. The proportion of the emitted N_2O contributed by nitrification and denitrification was then calculated from SP_0, according to Eq. 3, with SP_0 used in place of SP_{mean}.

For clarity, this approach to partitioning N_2O production pathways will hereafter be referred to as the CPM. Given the reported variability in endmember isotopic SP values for nitrification and denitrifying pathways (*18*, *86*), CPM was tested using a simulated isotopic data series with a Monte Carlo approach (see section S1.3.3). The method was found to perform well, particularly when fluxes showed little variability in the modeled window (12 hours), and when reduction was low (usually <10% in this study). Uncertainty in partitioning N_2O pathways using CPM would also be higher in situations where denitrification and nitrification contributions are approximately equal, as numerous minor N_2O production pathways produce N_2O with an SP in this intermediate range (*59*).

CPM results in some "smearing" of the distinction between different pathways across time because of the 12-hour window used for each calculation. However, multiple measurements are needed to partition between three possible pathways; therefore, this is the best approach possible with the available data. CPM can perform poorly when pathways—particularly reduction—are highly variable within a 12-hour window. We found that N_2O fluxes did not vary strongly within most 12-hour data periods (see Results); therefore, we assume that pathways are not highly variable at this time scale. Future studies using higher measurement time resolution—for example, when instrumental precision improvements allow source isotopic composition calculation with shorter chamber closure—will allow shorter CPM windows and thus improve temporal resolution of pathway calculations.

Soil sampling and ancillary measurements

Biomass growth

In order for the automated chambers to open and close properly, the height of plant biomass was maintained at <10 cm above the chamber collars. Therefore, each week of the experiment, biomass was cut to the top of the chamber collar, dried for 4 to 5 days at 80°C, and weighed. Following the end of the measurement period, on 12 November 2018, all dead and living biomass was removed down to the soil surface and grouped according to dead grasses, dead forbs, live grasses, and live forbs—subsampled to the main alpine genera *Cirsium* sp., *Plantago* sp., *Rumex* sp., *Geum* sp., *Leontodon* sp., *Trifolium* sp., and other forbs. The weight wet and dry weight (4 to 5 days at 80°C) of each plant group were measured for each monolith.

Soil sampling during the experiment

A week after fertilization on 12 July 2018, as well as several days before and after each of the two rewetting events (on 31 August, 6 September, and 13 September 2018), soil sampling was conducted on the top 6 cm of soil within each collar using a 2.5-cm-diameter core for the analysis of soil N isotopic composition and microbial ecology (see table S1 for a summary of important dates). Holes created by sampling were filled with surrounding soil; no changes were seen in fluxes on soil sampling days, and all monoliths received the same treatment. Four grams of soil from each monolith was weighed, dried at 80°C for 3 days, and weighed again, before freezing at −18°C. Analyses for bulk $\delta^{15}N$, $\delta^{13}C$, and C and N were performed at the Department of Microbiology and Ecosystem Science, University of Vienna, using EA-IRMS (Elemental Analyzer Isotope Ratio Mass Spectrometry).

Soil sampling after the experiment

After the biomass was collected, the monoliths were destructively sampled on 19 and 20 November 2018 into three depth layers (0 to 6, 6 to 12, 12 to 18 cm depth) to gain detailed information on soil physical and chemical properties. A HYPROP sampling core was taken at the 0- to 6-cm and 6- to 12-cm depths and stored in the refrigerator at 4°C for several months before analysis of the soil moisture retention using HYPROP 2 instrumentation (METER Group Inc. USA). HYPROP instrumentation uses two high-precision tensiometers inserted into a soil core to monitor soil water potential as a saturated soil sample dries, thus allowing accurate and fast measurement of the moisture release curve.

A 6-cm-deep soil core with radius 14 mm (approximately 40 g) was taken at each depth in each monolith and dried for 24 hours at 105°C before weighing to determine the soil bulk density. A 1- to 2-g subsample of the dried soil was transferred to an Eppendorf Safe-Lock tube and ground for 5 min at 30 motions s^{-1} in TissueLyser (QIAGEN Inc., USA). Subsamples (3 to 5 mg) were taken for measurements of total soil C and N using an elemental analyzer ("FlashEA 1112", Thermo Fisher Scientific, MA, USA) with the standard NC Soils configuration.

Soil NH_4^+ and NO_3^- nitrogen isotopic composition

For soil samples taken during the experiment (see the "Soil sampling during the experiment" section), 3 g of soil was weighed and immediately extracted in 1 M KCl (N-free, EMSURE, Merck KGgA) for 30 min while being shaken with 250 motions min^{-1}. The extracts were then filtered (Munktell folded filter paper, 80 g m^{-2}) and frozen at −18°C. In addition, leachate was periodically collected from the base of the monolith steel containers and frozen at −18°C. For both extracts and leachates, NH_4^+ and NO_3^- concentration and $\delta^{15}N$ isotopic composition were measured at the Department of Microbiology and Ecosystem Science, University of Vienna. NH_4^+ and NO_3^- concentration were determined colorimetrically, by measuring the spectrophotometric absorbance. For isotopic analysis, NH_4^+ was isolated from the extracts using microdiffusion and analyzed with EA-IRMS (*90*, *91*). Isotopic analysis of $\delta^{15}N - NO_3^-$ was conducted with PT-IRMS (Purge-and-Trap Isotope Ratio Mass Spectrometry) (*90*, *91*).

Functional gene analyses

For soil samples taken during the experiment (see the "Soil sampling during the experiment" section), 1 to 2 g of fresh soil were immediately frozen at −18°C in Eppendorf Safe-Lock PCR Clean tubes for microbial ecology analysis at the Helmholtz Zentrum München. DNA extraction was performed as described in (*92*) and (*93*) using a phenol/chloroform/isoamylalcohol mixture. qPCR was used to measure overall bacterial abundance [16*S* ribosomal RNA (rRNA) gene] and the abundances of key marker genes relating to the nitrogen cycle: *amoA* (AOA), *amoA* (AOB), *nirK, nirS, nosZ*, and *nifH*. qPCR protocols and primers are described in (*94*) for the N-cycle genes and in (*95*) for the 16*S* rRNA gene. To avoid PCR inhibition, the optimal DNA extract dilution (functional genes 1:256, 16*S* rRNA gene 1:4096) was determined by a dilution series qPCR. The R^2 of all standard curves was above 0.99, and the efficiencies of the amplification were as follows: 91.3% amoA (AOA), 81.6% amoA (AOB), 93.3% nirK, 81.7% nirS, 94.1% nosZ, 83.7% nifH, and 96.8% 16*S* rRNA gene.

NanoSIMS measurements

Soil samples collected before the drought, at peak drought, and a couple of days after rewetting (see the "Soil sampling during the experiment" section and table S1) were used for NanoSIMS analysis. Samples were held at −18°C until 8 months after collection, when they were prepared for NanoSIMS analysis. A tiny (<mg) amount of frozen soil was placed in a petri dish using tweezers, and 15 μl of isopropanol was added. Six microliters of isopropanol with suspended soil grains was picked up with a micropipette and dropped onto a 5 mm × 5 mm silicon wafer (Agar Scientific, UK), similarly to (*46*) and (*47*). The isopropanol was dried, and the soil grains remained adhered to the silicon wafer. A 10-nm platinum coating was added before measurements to improve sample conductivity and reduce lateral charging. Only a subset of samples were analyzed with the NanoSIMS (see table S3), as NanoSIMS measurements and data analysis are extremely time-consuming and expensive.

Measurements were performed with NanoSIMS 50L (CAMECA, France) at the Photon Science Institute, University of Manchester. This ion microprobe can provide extremely high lateral resolution as well as depth resolution for up to seven ion masses using a multicollector system to simultaneously achieve high mass resolution, sensitivity, and precision, as well as detection of the ion-induced secondary electrons (SE). In this study, a 16-keV Cs^+ beam with a beam current of 0.7 to 0.8 pA (D1-4) and ~0.3 pA (D1-5) was scanned over the surface to generate negative secondary ions ($^{12}C^-$, $^{16}O^-$, $^{12}C_2^-$, $^{12}C^{14}N^-$, $^{28}Si^-$, $^{32}S^-$, and $^{14}N^{16}O_2^-$) (*48*) that were analyzed in a double-focusing mass spectrometer. Before image collection, a 5×10^{15} Cs atom cm^{-2} implantation dose was used to achieve steady state and sputter away the Pt coating. Large-area scans with a 30 × 30 μm raster over 256 × 256 pixels containing numerous particles were taken at several positions for each sample with 200 μs $pixel^{-1}$ dwell time and D1-4, ES-3, AS-2, and EnS-open. Smaller areas with a raster size of 3 to 10 μm were acquired to gain information in depth for single particles. The NanoSIMS tuning for depth analysis was 256 × 256 or 128 × 128 pixels, dwell time 200/500/1000 μs $pixel^{-1}$ according to D1 aperture position, D1-4, or D1-5; other slits were the same as for the large-area scans. ImageJ with the OpenMIMS plugin (Harvard, Cambridge, MA, USA) was used for data analysis. Regions of interest corresponding to each particle visible in larger raster images or single particles in small raster images (*96*) were defined using OpenMIMS and used to measure the ion intensity in each analysis layer, as well as ion ratios for ions of interest. A total of 218 individual grains were defined as regions of interest and analyzed with OpenMIMS to produce the results shown in Fig. 3 and table S3. The depth scale in NanoSIMS sputtering layers (Fig. 3) cannot be easily converted into nanometers without extensive further study of the soil matrix, which is beyond the scope of this paper (*96*); thus, the depth scale is shown as a relative depth normalized for differing dwell times.

Statistics

To compare overall differences within a treatment at different time steps, e.g., D monoliths pre-drought and peak drought, and to compare differences between treatments at the same time step, e.g., C and D at peak drought, analysis of variance (ANOVA) was used on data from the 16 monoliths with a cutoff significance level of $P < 0.05$. When comparing particular treatment times/groups, Wilcoxon signed-rank and rank-sum tests for nonparametric data were applied. Cutoffs for *P* values were included throughout this paper as a guide to the reader; however, when *P* values were close to cutoffs, they are reported directly and considered closely. Context of the results including previous research and consistent patterns across independent methods were used to interpret results and reach major conclusions as recommended by (*97*). A PCA was used to look at causes of variability in the data. This was applied to two periods of the dataset: The initial (pre-drought) period from 7 to 14 July 2018, comprising a total of 626 data points, and the combined peak drought (26 August 2018 to 2 or 10 September 2018 for D1 and D2, respectively) and rewetting periods (3 or 11 September 2018 to +5 days), comprising 1186 data points. Data were normalized to a range between 0 and 1 before performing the PCA using the R function prcomp (*98*). All statistical analyses were performed using R 3.5.1 (*98*).

The experimental design in this study accounts for the variability of a natural grassland by using four monoliths for C and W treatments and seven for D treatments (D1 = 4 and D2 = 3). Monoliths (>50 to 100) would ideally be needed to cover the true variability in N_2O fluxes [e.g., 100+ plot replicates (*99*, *100*)], which is beyond the scope of this study. However, the high measurement frequency in this study can counterbalance the relatively low spatial measurement intensity (*99*), particularly considering the high temporal variability of N_2O emissions, as we report 1 to 2 orders of magnitude more data points for N_2O source isotopic composition than have been previously published [e.g., (*87*), (*40*)]. In addition, the use of two time points for both fertilization and rewetting accounts for the high variability of N_2O fluxes in response to current meterological and microclimatic conditions.

SUPPLEMENTARY MATERIALS

Supplementary material for this article is available at http://advances.sciencemag.org/cgi/content/full/7/6/eabb7118/DC1

REFERENCES AND NOTES

1. A. R. Ravishankara, J. S. Daniel, R. W. Portmann, Nitrous oxide (N_2O): The dominant ozone-depleting substance emitted in the 21st century. *Science* **326**, 123–125 (2009).
2. S. A. Montzka, E. J. Dlugokencky, J. H. Butler, Non-CO_2 greenhouse gases and climate change. *Nature* **476**, 43–50 (2011).
3. IPCC, *Climate Change 2014: Synthesis Report. Contribution of Working Groups I, II and III to the Fifth Assessment Report of the Intergovernmental Panel on Climate Change* (IPCC, 2014).
4. E. A. Davidson, The contribution of manure and fertilizer nitrogen to atmospheric nitrous oxide since 1860. *Nat. Geosci.* **2**, 659–662 (2009).
5. S. Park, P. Croteau, K. A. Boering, D. M. Etheridge, D. Ferretti, P. J. Fraser, K.-R. Kim, P. B. Krummel, R. L. Langenfelds, T. D. van Ommen, L. P. Steele, C. M. Trudinger, Trends

and seasonal cycles in the isotopic composition of nitrous oxide since 1940. *Nat. Geosci.* **5**, 261–265 (2012).
6. World Bank, *World Development Indicators: Fertiliser Consumption (AG.CON.FERT.ZS)* (World Bank, 2019).
7. H. Tian, J. Yang, R. Xu, C. Lu, J. G. Canadell, E. A. Davidson, R. B. Jackson, A. Arneth, J. Chang, P. Ciais, S. Gerber, A. Ito, F. Joos, S. Lienert, P. Messina, S. Olin, S. Pan, C. Peng, E. Saikawa, R. L. Thompson, N. Vuichard, W. Winiwarter, S. Zaehle, B. Zhang, Global soil nitrous oxide emissions since the preindustrial era estimated by an ensemble of terrestrial biosphere models: Magnitude, attribution, and uncertainty. *Glob. Chang. Biol.* **25**, 640–659 (2019).
8. E. J. Dlugokencky (2019); NOAA/GML (www.esrl.noaa.gov/gmd/ccgg/trends_n2o/).
9. R. L. Thompson, L. Lassaletta, P. K. Patra, C. Wilson, K. C. Wells, A. Gressent, E. N. Koffi, M. P. Chipperfield, W. Winiwarter, E. A. Davidson, H. Tian, J. G. Canadell, Acceleration of global N_2O emissions seen from two decades of atmospheric inversion. *Nat. Clim. Change* **9**, 993–998 (2019).
10. R. G. Prinn, R. F. Weiss, J. Arduini, T. Arnold, H. L. De Witt, P. J. Fraser, A. L. Ganesan, J. Gasore, C. M. Harth, O. Hermansen, J. Kim, P. B. Krummel, S. Li, Z. M. Loh, C. R. Lunder, M. Maione, A. J. Manning, B. R. Miller, B. Mitrevski, J. Mühle, S. O'Doherty, S. Park, S. Reimann, M. Rigby, T. Saito, P. K. Salameh, R. Schmidt, P. G. Simmonds, L. P. Steele, M. K. Vollmer, R. H. Wang, B. Yao, Y. Yokouchi, D. Young, L. Zhou, History of chemically and radiatively important atmospheric gases from the Advanced Global Atmospheric Gases Experiment (AGAGE). *Earth Sys. Sci. Data* **10**, 985–1018 (2018).
11. T. J. Griffis, Z. Chen, J. M. Baker, J. D. Wood, D. B. Millet, X. Lee, R. T. Venterea, P. A. Turner, Nitrous oxide emissions are enhanced in a warmer and wetter world. *Proc. Natl. Acad. Sci. U.S.A.* **114**, 12081–12085 (2017).
12. F. Ehrhardt, J.-F. Soussana, G. Bellocchi, P. Grace, R. M. Auliffe, S. Recous, R. Sándor, P. Smith, V. Snow, M. de Antoni Migliorati, B. Basso, A. Bhatia, L. Brilli, J. Doltra, C. D. Dorich, L. Doro, N. Fitton, S. J. Giacomini, B. Grant, M. T. Harrison, S. K. Jones, M. U. F. Kirschbaum, K. Klumpp, P. Laville, J. Léonard, M. Liebig, M. Lieffering, R. Martin, R. S. Massad, E. Meier, L. Merbold, A. D. Moore, V. Myrgiotis, P. Newton, E. Pattey, S. Rolinski, J. Sharp, W. N. Smith, L. Wu, Q. Zhang, Assessing uncertainties in crop and pasture ensemble model simulations of productivity and N_2O emissions. *Glob. Chang. Biol.* **24**, e603–e616 (2018).
13. K. Butterbach-Bahl, E. M. Baggs, M. Dannenmann, R. Kiese, S. Zechmeister-Boltenstern, Nitrous oxide emissions from soils: How well do we understand the processes and their controls? *Philos. Trans. R. Soc. B* **368**, 20130122 (2013).
14. N. Wrage, G. L. Velthof, M. L. V. Beusichem, O. Oenema, Role of nitrifier denitrification in the production of nitrous oxide. *Soil Biol. Biogeochem.* **123**, A3–A16 (2018).
15. O. Spott, R. Russow, C. F. Stange, Formation of hybrid N_2O and hybrid N_2 due to codenitrification: First review of a barely considered process of microbially mediated N-nitrosation. *Soil Biol. Biochem.* **43**, 1995–2011 (2011).
16. T. J. Clough, G. J. Lanigan, C. A. M. de Klein, S. Samad, S. E. Morales, D. Rex, L. R. Bakken, C. Johns, L. M. Condron, J. Grant, K. G. Richards, Influence of soil moisture on codenitrification fluxes from a urea-affected pasture soil. *Sci. Rep.* **7**, 2185 (2017).
17. J. Wei, M. Zhou, H. Vereecken, N. Brüggemann, Large variability in CO_2 and N_2O emissions and in ^{15}N site preference of N_2O from reactions of nitrite with lignin and its derivatives at different pH. *Rapid Commun. Mass Spectrom.* **31**, 1333–1343 (2017).
18. D. Lewicka-Szczebak, J. Augustin, A. Giesemann, R. Well, Quantifying N_2O reduction to N_2 based on N_2O isotopocules-validation with independent methods (helium incubation and ^{15}N gas flux method). *Biogeosciences* **14**, 711–732 (2017).
19. D. Wu, R. Well, L. M. Cárdenas, R. Fuß, D. Lewicka-Szczebak, J. R. Köster, N. Brüggemann, R. Bol, Quantifying N_2O reduction to N_2 during denitrification in soils via isotopic mapping approach: Model evaluation and uncertainty analysis. *Environ. Res.* **179**, 108806 (2019).
20. E. Bai, B. Z. Houlton, Y. P. Wang, Isotopic identification of nitrogen hotspots across natural terrestrial ecosystems. *Biogeosciences* **9**, 3287–3304 (2012).
21. L. Yu, E. Harris, S. Henne, S. Eggleston, M. Steinbacher, L. Emmenegger, C. Zellweger, J. Mohn, Atmospheric nitrous oxide isotopes observed at the high-altitude research station Jungfraujoch, Switzerland. *Atmos. Chem. Phys.* **20**, 6495–6519 (2020).
22. A. Dai, Increasing drought under global warming in observations and models. *Nat. Clim. Change* **3**, 52–58 (2013).
23. A. Dai, T. Zhao, Uncertainties in historical changes and future projections of drought. Part I: Estimates of historical drought changes. *Clim. Change* **144**, 519–533 (2017).
24. T. Zhao, A. Dai, Uncertainties in historical changes and future projections of drought. Part II: Model-simulated historical and future drought changes. *Clim. Change* **144**, 535–548 (2017).
25. M. Reichstein, M. Bahn, P. Ciais, D. Frank, M. D. Mahecha, S. I. Seneviratne, J. Zscheischler, C. Beer, N. Buchmann, D. C. Frank, D. Papale, A. Rammig, P. Smith, K. Thonicke, M. van der Velde, S. Vicca, A. Walz, M. Wattenbach, Climate extremes and the carbon cycle. *Nature* **500**, 287–295 (2013).
26. D. Frank, M. Reichstein, M. Bahn, K. Thonicke, D. Frank, M. D. Mahecha, P. Smith, M. van der Velde, S. Vicca, F. Babst, C. Beer, N. Buchmann, J. G. Canadell, P. Ciais, W. Cramer, A. Ibrom, F. Miglietta, B. Poulter, A. Rammig, S. I. Seneviratne, A. Walz, M. Wattenbach, M. A. Zavala, J. Zscheischler, Effects of climate extremes on the terrestrial carbon cycle: Concepts, processes and potential future impacts. *Glob. Chang. Biol.* **21**, 2861–2880 (2015).
27. E. L. Aronson, M. L. Goulden, S. D. Allison, Greenhouse gas fluxes under drought and nitrogen addition in a Southern California grassland. *Soil Biol. Biochem.* **131**, 19–27 (2019).
28. A. Kübert, M. Götz, E. Kuester, A. Piayda, C. Werner, Y. Rothfuss, M. Dubbert, Nitrogen loading enhances stress impact of drought on a semi-natural temperate grassland. *Front. Plant Sci.* **10**, 1051 (2019).
29. L. V. Verchot, E. A. Davidson, H. Cattânio, I. L. Ackerman, H. E. Erickson, M. Keller, Land use change and biogeochemical controls of nitrogen oxide emissions from soils in eastern Amazonia. *Global Biogeochem. Cycles* **13**, 31–46 (1999).
30. E. A. Davidson, F. Y. Ishida, D. C. Nepstad, Effects of an experimental drought on soil emissions of carbon dioxide, methane, nitrous oxide, and nitric oxide in a moist tropical forest. *Glob. Chang. Biol.* **10**, 718–730 (2004).
31. L. Chapuis-Lardy, N. Wrage, A. Metay, J. L. Chotte, M. Bernoux, Soils, a sink for N_2O? A review. *Glob. Change Biol.* **13**, 1–17 (2007).
32. W. Borken, E. Matzner, Reappraisal of drying and wetting effects on C and N mineralization and fluxes in soils. *Glob. Chang. Biol.* **15**, 808–824 (2009).
33. L. Fuchslueger, M. Bahn, K. Fritz, R. Hasibeder, A. Richter, Experimental drought reduces the transfer of recently fixed plant carbon to soil microbes and alters the bacterial community composition in a mountain meadow. *New Phytol.* **201**, 916–927 (2014).
34. X. Xu, Y. Ran, Y. Li, Q. Zhang, Y. Liu, H. Pan, X. Guan, J. Li, J. Shi, L. Dong, Z. Li, H. Di, J. Xu, Warmer and drier conditions alter the nitrifier and denitrifier communities and reduce N_2O emissions in fertilized vegetable soils. *Agric. Ecosyst. Environ.* **231**, 133–142 (2016).
35. P. M. Homyak, S. D. Allison, T. E. Huxman, M. L. Goulden, K. K. Treseder, Effects of drought manipulation on soil nitrogen cycling: A meta-analysis. *J. Geophys. Res. Biogeo.* **122**, 3260–3272 (2017).
36. A. Canarini, F. A. Dijkstra, Dry-rewetting cycles regulate wheat carbon rhizodeposition, stabilization and nitrogen cycling. *Soil Biol. Biochem.* **81**, 195–203 (2015).
37. A. Priemé, S. Christensen, Natural perturbations, drying–wetting and freezing–thawing cycles, and the emission of nitrous oxide, carbon dioxide and methane from farmed organic soils. *Soil Biol. Biochem.* **33**, 2083–2091 (2001).
38. S. D. Goldberg, G. Gebauer, Drought turns a Central European Norway spruce forest soil from an N_2O source to a transient N_2O sink. *Glob. Chang. Biol.* **15**, 850–860 (2009).
39. D.-G. Kim, R. Vargas, B. Bond-Lamberty, M. R. Turetsky, Effects of soil rewetting and thawing on soil gas fluxes: A review of current literature and suggestions for future research. *Biogeosciences* **9**, 2459–2483 (2012).
40. E. Ibraim, B. Wolf, E. Harris, R. Gasche, J. Wei, L. Yu, R. Kiese, S. Eggleston, K. Butterbach-Bahl, M. Zeeman, B. Tuzson, L. Emmenegger, J. Six, S. Henne, J. Mohn, Attribution of N_2O sources in a grassland soil with laser spectroscopy based isotopocule analysis. *Biogeosciences* **16**, 3247–3266 (2019).
41. E. Verhoeven, M. Barthel, L. Yu, L. Celi, D. Said-Pullicino, S. Sleutel, D. Lewicka-Szczebak, J. Six, C. Decock, Early season N_2O emissions under variable water management in rice systems: Source-partitioning emissions using isotope ratios along a depth profile. *Biogeosciences* **16**, 383–408 (2019).
42. E. Harris, A. Joss, L. Emmenegger, M. Kipf, B. Wolf, J. Mohn, P. Wunderlin, Isotopic evidence for nitrous oxide production pathways in a partial nitritation-anammox reactor. *Water Res.* **83**, 258–270 (2015).
43. S. O. Petersen, R. Well, A. Taghizadeh-Toosi, T. J. Clough, Seasonally distinct sources of N_2O in acid organic soil drained for agriculture as revealed by N_2O isotopomer analysis. *Biogeochemistry* **147**, 15–33 (2020).
44. M. Holmstrup, C. Damgaard, I. K. Schmidt, M. F. Arndal, C. Beier, T. N. Mikkelsen, P. Ambus, K. S. Larsen, K. Pilegaard, A. Michelsen, L. C. Andresen, M. Haugwitz, L. Bergmark, A. Priemé, A. S. Zaitsev, S. Georgieva, M. Dam, M. Vestergård, S. Christensen, Long-term and realistic global change manipulations had low impact on diversity of soil biota in temperate heathland. *Sci. Rep.* **7**, 41388 (2017).
45. V. Hammerl, E.-M. Kastl, M. Schloter, S. Kublik, H. Schmidt, G. Welzl, A. Jentsch, C. Beierkuhnlein, S. Gschwendtner, Influence of rewetting on microbial communities involved in nitrification and denitrification in a grassland soil after a prolonged drought period. *Nat. Sci. Rep.* **9**, 2280 (2019).
46. L. Remusat, P.-J. Hatton, P. S. Nico, B. Zeller, M. Kleber, D. Derrien, NanoSIMS study of organic matter associated with soil aggregates: Advantages, limitations, and combination with STXM. *Environ. Sci. Tech.* **46**, 3943–3949 (2012).
47. C. Vogel, C. W. Mueller, C. Höschen, F. Buegger, K. Heister, S. Schulz, M. Schloter, I. Kögel-Knabner, Submicron structures provide preferential spots for carbon and nitrogen sequestration in soils. *Nat. Commun.* **5**, 2947 (2014).
48. K. Li, B. Sinha, P. Hoppe, Speciation of nitrogen-bearing species using negative and positive secondary ion spectra with nano secondary ion mass spectrometry. *Anal. Chem.* **88**, 3281–3288 (2016).
49. A. A. Hartmann, R. L. Barnard, S. Marhan, P. A. Niklaus, Effects of drought and N-fertilization on N cycling in two grassland soils. *Oecologia* **171**, 705–717 (2013).

50. S. Leitner, P. M. Homyak, J. C. Blankinship, J. Eberwein, G. D. Jenerette, S. Zechmeister-Boltenstern, J. P. Schimel, Linking NO and N_2O emission pulses with the mobilization of mineral and organic N upon rewetting dry soils. *Soil Biol. Biochem.* **115**, 461–466 (2017).
51. IPCC, *2006 IPCC Guidelines for National Greenhouse Gas Inventories* (IGES, 2006).
52. R. Well, H. Flessa, L. Xing, J. Xiaotang, V. Römheld, Isotopologue ratios of N_2O emitted from microcosms with NH_4^+ fertilized arable soils under conditions favoring nitrification. *Soil Biol. Biochem.* **40**, 2416–2426 (2008).
53. A. Castellano-Hinojosa, J. González-López, E. J. Bedmar, Distinct effect of nitrogen fertilisation and soil depth on nitrous oxide emissions and nitrifiers and denitrifiers abundance. *Biol. Fertil. Soils* **54**, 829–840 (2018).
54. J. P. Schimel, Life in dry soils: Effects of drought on soil microbial communities and processes. *Annu. Rev. Ecol. Evol. Syst.* **49**, 409–432 (2018).
55. K. A. Thorn, M. A. Mikita, Nitrite fixation by humic substances nitrogen-15 nuclear magnetic resonance evidence for potential intermediates in chemodenitrification. *Soil Sci. Soc. Am. J.* **64**, 568–582 (2000).
56. B.-R. Lee, R. Zaman, J.-C. Avice, A. Ourry, T.-H. Kim, Sulfur use efficiency is a significant determinant of drought stress tolerance in relation to photosynthetic activity in *Brassica napus* cultivars. *Front. Plant Sci.* **7**, 459 (2016).
57. G. J. Burch, I. D. Moore, J. Burns, Soil hydrophobic effects on infiltration and catchment runoff. *Hydrol. Process.* **3**, 211–222 (1989).
58. A. Sowerby, B. A. Emmett, A. Tietema, C. Beier, Contrasting effects of repeated summer drought on soil carbon efflux in hydric and mesic heathland soils. *Glob. Chang. Biol.* **14**, 2388–2404 (2008).
59. L. Yu, E. Harris, D. Lewicka-Szczebak, J. Mohn, What can we learn from N_2O isotope data? - Analytics, processes and modelling. *Rapid Commun. Mass Spectrom.* **34**, e8858 (2020).
60. J. Wei, E. Ibraim, N. Brüggemann, H. Vereecken, J. Mohn, First real-time isotopic characterisation of N_2O from chemodenitrification. *Geochim. Cosmochim. Acta* **267**, 17–32 (2019).
61. J. Kreyling, A. H. Schweiger, M. Bahn, P. Ineson, M. Migliavacca, T. Morel-Journel, J. R. Christiansen, N. Schtickzelle, K. S. Larsen, To replicate, or not to replicate—That is the question: How to tackle nonlinear responses in ecological experiments. *Ecol. Lett.* **21**, 1629–1638 (2018).
62. H. F. Birch, Mineralization of plant nitrogen following alternate wet and dry conditions. *Plant Soil* **20**, 43–49 (1964).
63. J. Ingrisch, S. Karlowsky, A. Anadon-Rosell, R. Hasibeder, A. König, A. Augusti, G. Gleixner, M. Bahn, Land use alters the drought responses of productivity and CO_2 fluxes in mountain grassland. *Ecosystems* **21**, 689–703 (2018).
64. R. T. Venterea, Nitrite-driven nitrous oxide production under aerobic soil conditions: Kinetics and biochemical controls. *Glob. Chang. Biol.* **13**, 1798–1809 (2007).
65. J. Wei, W. Amelung, E. Lehndorff, M. Schloter, H. Vereecken, N. Brüggemann, N_2O and NO_x emissions by reactions of nitrite with soil organic matter of a Norway spruce forest. *Biogeochemistry* **132**, 325–342 (2017).
66. M. Prokopiou, P. Martinerie, C. J. Sapart, E. Witrant, G. Monteil, K. Ishijima, S. Bernard, J. Kaiser, I. Levin, T. Blunier, D. Etheridge, E. Dlugokencky, R. S. W. van de Wal, T. Röckmann, Constraining N_2O emissions since 1940 using firn air isotope measurements in both hemispheres. *Atmos. Chem. Phys.* **17**, 4539–4564 (2017).
67. J. W. Erisman, M. A. Sutton, J. Galloway, Z. Klimont, W. Winiwarter, How a century of ammonia synthesis changed the world. *Nat. Geosci.* **1**, 636–639 (2008).
68. A. E. Davidson, P. A. Matson, P. M. Vitousek, R. Riley, K. Dunkin, C. Garcia-Mendez, J. M. Maass, Processes regulating soil emissions of NO and N^2O in a seasonally dry tropical forest. *Ecology* **74**, 130–139 (1993).
69. R. Ruser, H. Flessa, R. Russow, G. Schmidt, F. Buegger, J. C. Munch, Emission of N_2O, N_2 and CO_2 from soil fertilized with nitrate: Effect of compaction, soil moisture and rewetting. *Soil Biol. Biochem.* **38**, 263–274 (2006).
70. E. Harris, T. Ladreiter-Knauss, K. Butterbach-Bahl, B. Wolf, M. Bahn, Land-use and abandonment alters methane and nitrous oxide fluxes in mountain grasslands. *Sci. Total Environ.* **628-629**, 997–1008 (2018).
71. M. Bahn, M. Schmitt, R. Siegwolf, A. Richter, N. Brüggemann, Does photosynthesis affect grassland soil-respired CO_2 and its carbon isotope composition on a diurnal timescale? *New Phytol.* **182**, 451–460 (2009).
72. S. Meyer, J. Leifeld, M. Bahn, J. Fuhrer, Land-use change in subalpine grassland soils: Effect on particulate organic carbon fractions and aggregation. *J. Plant Nutr. Soil Sci.* **175**, 401–409 (2012).
73. L. Fuchslueger, E.-M. Kastl, F. Bauer, S. Kienzl, R. Hasibeder, T. Ladreiter-Knauss, M. Schmitt, M. Bahn, M. Schloter, A. Richter, U. Szukics, Effects of drought on nitrogen turnover and abundances of ammonia-oxidizers in mountain grassland. *Biogeosciences* **11**, 6003–6015 (2014).
74. H. J. De Boeck, S. Bassin, M. Verlinden, M. Zeiter, E. Hiltbrunner, Simulated heat waves affected alpine grassland only in combination with drought. *New Phytol.* **209**, 531–541 (2015).
75. H. J. De Boeck, E. Hiltbrunner, M. Verlinden, S. Bassin, M. Zeiter, Legacy effects of climate extremes in alpine grassland. *Front. Plant Sci.* **9**, 1586 (2018).
76. L. Fuchslueger, B. Wild, M. Mooshammer, M. Takriti, S. Kienzl, A. Knoltsch, F. Hofhansl, M. Bahn, A. Richter, Microbial carbon and nitrogen cycling responses to drought and temperature in differently managed mountain grasslands. *Soil Biol. Biochem.* **135**, 144–153 (2019).
77. I. J. Slette, A. K. Post, M. Awad, T. Even, A. Punzalan, S. Williams, M. D. Smith, A. K. Knapp, How ecologists define drought, and why we should do better. *Glob. Chang. Biol.* **25**, 3193–3200 (2019).
78. S. Toyoda, N. Kuroki, N. Yoshida, K. Ishijima, Y. Tohjima, T. Machida, Decadal time series of tropospheric abundance of N2O isotopomers and isotopologues in the northern hemisphere obtained by the long-term observation at Hateruma Island, Japan. *J. Geophys. Res. Atmos.* **118**, 3369–3381 (2013).
79. N. Pirk, M. Mastepanov, F.-J. Parmentier, M. Lund, P. Crill, T. R. Christensen, Calculations of automatic chamber flux measurements of methane and carbon dioxide using short time series of concentrations. *Biogeosciences* **13**, 903–912 (2016).
80. C. D. Keeling, The concentration and isotopic abundances of atmospheric carbon dioxide in rural areas. *Geochim. Cosmochim. Acta* **13**, 322–334 (1958).
81. C. D. Keeling, The concentration and isotopic abundances of carbon dioxide in rural and marine air. *Tellus* **24**, 277–298 (1960).
82. J. Mohn, W. Gutjahr, S. Toyoda, E. Harris, E. Ibraim, H. Geilmann, P. Schleppi, T. Kuhn, M. F. Lehmann, C. Decock, R. A. Werner, N. Yoshida, W. A. Brand, Reassessment of the NH_4NO_3thermal decomposition technique for calibration of the N_2O isotopic composition. *Rapid Commun. Mass Spectrom.* **30**, (2016).
83. J. Mohn, B. Tuzson, A. Manninen, N. Yoshida, S. Toyoda, W. A. Brand, L. Emmenegger, Site selective real-time measurements of atmospheric N_2O isotopomers by laser spectroscopy. *Atmos. Meas. Tech.* **5**, 1601–1609 (2012).
84. E. Harris, D. D. Nelson, W. Olszewski, M. Zahniser, K. E. Potter, B. J. McManus, A. Whitehill, R. G. Prinn, S. Ono, Development of a spectroscopic technique for continuous online monitoring of oxygen and site-specific nitrogen isotopic composition of atmospheric nitrous oxide. *Anal. Chem.* **86**, 1726–1734 (2014).
85. E. Harris, S. Henne, C. Hüglin, C. Zellweger, B. Tuzson, E. Ibraim, L. Emmenegger, J. Mohn, Tracking nitrous oxide emission processes at a suburban site with semicontinuous, in situ measurements of isotopic composition. *J. Geophys. Res. Atmos.* **122**, 1850–1870 (2017).
86. T. R. A. Denk, J. Mohn, C. Decock, D. Lewicka-Szczebak, E. Harris, K. Butterbach-Bahl, R. Kiese, B. Wolf, The nitrogen cycle: A review of isotope effects and isotope modeling approaches. *Soil Biol. Biochem.* **105**, 121–137 (2017).
87. B. Wolf, L. Merbold, C. Decock, B. Tuzson, E. Harris, J. Six, L. Emmenegger, J. Mohn, First on-line isotopic characterization of N_2O emitted from intensively managed grassland. *Biogeosciences* **12**, 2517–2531 (2015).
88. D. Wu, J. R. Köster, L. M. Cárdenas, N. Brüggemann, D. Lewicka-Szczebak, R. Bol, N2O source partitioning in soils using ^{15}N site preference values corrected for the N_2O reduction effect. *Rapid Commun. Mass Spectrom.* **30**, 620–626 (2016).
89. N. E. Ostrom, A. Pitt, R. Sutka, P. H. Ostrom, A. S. Grandy, K. M. Huizinga, G. P. Robertson, Isotopologue effects during N_2O reduction in soils and in pure cultures of denitrifiers. *J. Geophys. Res. Biogeosci.* **112**, G02005 (2007).
90. P. Lachouani, A. Frank, W. Wanek, A suite of sensitive chemical methods to determine the $\delta^{15}N$ of ammonium, nitrate and total dissolved N in soil extracts. *Rapid Commun. Mass Spectrom.* **24**, 3615–3623 (2010).
91. R. Hood-Nowotny, N. H.-N. Umana, E. Inselbacher, P. Oswald-Lachouani, W. Wanek, Alternative methods for measuring inorganic, organic, and total dissolved nitrogen in soil. *Soil Sci. Soc. Am. J.* **74**, 1018–1027 (2010).
92. T. Lueders, M. Manefield, M. W. Friedrich, Enhanced sensitivity of DNA- and rRNA-based stable isotope probing by fractionation and quantitative analysis of isopycnic centrifugation gradients. *Environ. Microbiol.* **6**, 73–78 (2004).
93. S. Töwe, S. Wallisch, A. Bannert, D. Fischer, B. Hai, F. Haesler, K. Kleineidam, M. Schloter, Improved protocol for the simultaneous extraction and column-based separation of DNA and RNA from different soils. *J. Microbiol. Methods* **84**, 406–412 (2011).
94. S. Töwe, A. Albert, K. Kleineidam, R. Brankatschk, A. Dümig, G. Welzl, J. C. Munch, J. Zeyer, M. Schloter, Abundance of microbes involved in nitrogen transformation in the rhizosphere of *Leucanthemopsis alpina* (L.) heywood grown in soils from different sites of the Damma glacier forefield. *Microb. Ecol.* **60**, 762–770 (2010).
95. S. Geschwendtner, J. Esperschütz, F. Buegger, M. Reichmann, M. Müller, J. C. Munch, M. Schloter, Effects of genetically modified starch metabolism in potato plants on photosynthate fluxes into the rhizosphere and on microbial degraders of root exudates. *FEMS Microbiol. Ecol.* **76**, 564–575 (2011).
96. C. W. Mueller, A. Kölbl, C. Hoeschen, F. Hillion, K. Heister, A. M. Herrmann, I. Kögel-Knabner, Submicron scale imaging of soil organic matter dynamics using NanoSIMS—From single particles to intact aggregates. *Org. Geochem.* **42**, 1476–1488 (2012).
97. V. Amrhein, S. Greenland, B. McShane, Scientists rise up against statistical significance. *Nature* **567**, 305–307 (2019).
98. R Core Team, *R: A Language and Environment for Statistical Computing* (R Foundation for Statistical Computing, 2017).

99. C. Arias-Navarro, E. Díaz-Pinés, S. Klatt, P. Brandt, M. C. Rufino, K. Butterbach-Bahl, L. V. Verchot, Spatial variability of soil N_2O and CO_2 fluxes in different topographic positions in a tropical montane forest in Kenya. *J. Geophys. Res. Biogeo.* **122**, 514–527 (2017).
100. D. A. Turner, D. Chen, I. E. Galbally, R. Leuning, R. B. Edis, Y. Li, K. Kelly, F. Phillips, Spatial variability of nitrous oxide emissions from an Australian irrigated dairy pasture. *Plant Soil* **309**, 77–88 (2008).
101. R. G. Prinn, R. F. Weiss, P. J. Fraser, P. G. Simmonds, D. M. Cunnold, F. N. Alyea, S. O'Doherty, P. Salameh, B. R. Miller, J. Huang, R. H. J. Wang, D. E. Hartley, C. Harth, L. P. Steele, G. Sturrock, P. M. Midgley, A. McCulloch, A history of chemically and radiatively important gases in air deduced from ALE/GAGE/AGAGE. *J. Geophys. Res. Atmos.* **105**, 17751–17792 (2000).
102. R. G. Prinn, R. F. Weiss, P. J. Fraser, P. G. Simmonds, D. M. Cunnold, S. J. O'Doherty, P. K. Salameh, L. W. Porter, P. B. Krummel, R. H. J. Wang, B. R. Miller, C. Harth, B. R. Greally, V. Woy, F.A., L. P. Steele, J. Mühle, W. T. Sturges, F. N. Alyea, J. Huang, D. E. Hartley, *The ALE/GAGE AGAGE Network* (2013); doi: 10.3334/CDIAC/atg.db1001.
103. R. L. Sutka, N. E. Ostrom, P. H. Ostrom, H. Gandhi, J. A. Breznak, Erratum: Nitrogen isotopomer site preference of N_2O produced by *Nitrosomonas europaea* and *Methylococcus capsulatus* Bath. *Rapid Commun. Mass Spectrom.* **18**, 1411–1412 (2004).
104. R. L. Sutka, N. E. Ostrom, P. H. Ostrom, J. A. Breznak, H. Gandhi, A. J. Pitt, F. Li, Distinguishing nitrous oxide production from nitrification and denitrification on the basis of isotopomer abundances. *Appl. Environ. Microbiol.* **72**, 638–644 (2006).
105. S. Toyoda, H. Mutobe, H. Yamagishi, N. Yoshida, Y. Tanji, Fractionation of N_2O isotopomers during production by denitrifier. *Soil Biol. Biochem.* **37**, 1535–1545 (2005).
106. S. Toyoda, M. Yano, S.-i. Nishimura, H. Akiyama, A. Hayakawa, K. Koba, S. Sudo, K. Yagi, A. Makabe, Y. Tobari, N. O. Ogawa, N. Ohkouchi, K. Yamada, N. Yoshida, Characterization and production and consumption processes of N_2O emitted from temperate agricultural soils determined via isotopomer ratio analysis. *Global Biogeochem. Cycles* **25**, GB2008 (2011).
107. P. Wunderlin, M. F. Lehmann, H. Siegrist, B. Tuzson, A. Joss, L. Emmenegger, J. Mohn, Isotope signatures of N_2O in a mixed microbial population system: Constraints on N_2O producing pathways in wastewater treatment. *Environ. Sci. Technol.* **47**, 1339–1348 (2013).
108. J. Heil, B. Wolf, N. Brüggemann, L. Emmenegger, B. Tuzson, H. Vereecken, J. Mohn, Site-specific ^{15}N signatures of abiotically-produced N_2O. *Geochim. Cosmochim. Acta* **139**, 72–82 (2014).
109. A. Schilt, E. J. Brook, T. K. Bauska, D. Baggenstos, H. Fischer, F. Joos, V. V. Petrenko, H. Schaefer, J. Schmitt, J. P. Severinghaus, R. Spahni, T. F. Stocker, Isotopic constraints on marine and terrestrial N_2O emissions during the last deglaciation. *Nature* **516**, 234–237 (2014).
110. J. Mohn, B. Wolf, S. Toyoda, C.-T. Lin, M.-C. Liang, N. Brüggemann, H. Wissel, A. E. Steiker, J. Dyckmans, L. Szwec, N. E. Ostrom, K. L. Casciotti, M. Forbes, A. Giesemann, R. Well, R. R. Doucett, C. T. Yarnes, A. R. Ridley, J. Kaiser, N. Yoshida, Interlaboratory assessment of nitrous oxide isotopomer analysis by isotope ratio mass spectrometry and laser spectroscopy: Current status and perspectives. *Rapid Commun. Mass Spectrom.* **28**, 1995–2007 (2014).

Acknowledgments: We thank E. Dlugokencky and the NOAA HATS/CCGG program for contribution of the flask data for the Barrow station and P. Krummel and the AGAGE network for data from the Cape Grim station as shown in fig. S1, as well as the ZAMG (Zentralanstalt für Meteorologie und Geodynamik, Austria) and the University of Innsbruck for precipitation data shown in fig. S6. We also thank J. Mohn (Empa, Switzerland) for provision of standard gases and assistance with international isotope scale calibration and A. Richter and W. Wanek (University of Vienna) for the measurements of soil N isotopic composition. **Funding:** This work was supported by the Austrian Science Foundation (FWF) project P31132 "NitroTrace: Using isotopes to trace the effects of climate extremes on N_2O emissions and the nitrogen cycle in managed grasslands," the Austrian Research Promotion Agency (FFG) project "LTER-CWN: Long-Term Ecosystem Research Infrastructure for Carbon, Water and Nitrogen," and the Tiroler Wissenschaftsfonds (TWF) 2018 grant for the project "An isotopic investigation into the effects of drought and rewetting on nitrous oxide production pathways in a mountain grassland." **Author contributions:** E.H. and M.B. planned this project and wrote the manuscript with extensive comments and contribution from E.D.-P. and N.B.; E.H. carried out isotope measurements and analyzed the data; E.S. performed soil N isotope measurements; E.H., E.D.-P., S.Z.-B., S.G., and M.B. were responsible for infrastructure development in the LTER-CWN project; M.S., S.S., and C.D. carried out microbial analyses and discussed microbial data; K.L. and K.L.M. performed NanoSIMS analyses and assisted with interpretation of results; and E.S., J.I., and D.R. provided support for laboratory and field work activities. **Competing interests:** The authors declare that they have no competing interests. **Data and materials availability:** N_2O isotopocule and flux data as well as CH_4 and CO_2 fluxes from chamber measurements and all soil and microbial ancillary data described in Materials and Methods will be made publicly available on the Pangaea database (https://doi.org/10.1594/PANGAEA.907601). NanoSIMS results will be made available upon request to E.H. (eliza.harris@uibk.ac.at); file size and format precludes addition to the Pangaea database.

Submitted 12 March 2020
Accepted 7 December 2020
Published 5 February 2021
10.1126/sciadv.abb7118

Citation: E. Harris, E. Diaz-Pines, E. Stoll, M. Schloter, S. Schulz, C. Duffner, K. Li, K. L. Moore, J. Ingrisch, D. Reinthaler, S. Zechmeister-Boltenstern, S. Glatzel, N. Brüggemann, M. Bahn, Denitrifying pathways dominate nitrous oxide emissions from managed grassland during drought and rewetting. *Sci. Adv.* **7**, eabb7118 (2021).

ScienceAdvances

Denitrifying pathways dominate nitrous oxide emissions from managed grassland during drought and rewetting

E. HarrisE. Diaz-PinesE. StollM. SchloterS. SchulzC. DuffnerK. LiK. L. MooreJ. IngrischD. ReinthalerS. Zechmeister-BoltensternS. GlatzelN. BrüggemannM. Bahn

Sci. Adv., 7 (6), eabb7118. • DOI: 10.1126/sciadv.abb7118

Science Advances (ISSN 2375-2548) is published by the American Association for the Advancement of Science. 1200 New York Avenue NW, Washington, DC 20005. The title *Science Advances* is a registered trademark of AAAS.